A Copernicus-based evapotranspiration dataset at 100-m spatial resolution over the Mediterranean region

Paulina Bartkowiak[1], Bartolomeo Ventura[1], Alexander Jacob[1], Mariapina Castelli[1]

[1]Insitute for Earth Observation, EURAC Research, Bozen-Bolzano, 39110, Italy

5   *Correspondence to*: Paulina Bartkowiak (paulina.bartkowiak@eurac.edu)

Abstract. Evapotranspiration (ET) is responsible for regulating the hydrological cycle with a relevant impact on air humidity and precipitation, particularly important in the context of acute drought events in recent years. With the intensification of rainfall deficits and extreme heat events, the Mediterranean region requires regular monitoring to enhance water resources management. Even though remote sensing provides spatially continuous information for estimating ET on large scales, existing
10   global products with spatial resolution ≥ 0.5 km are insufficient to capture spatial detail at a local level. In the framework of the ESA 4DMed-Hydrology project, we generate an ET dataset at both high spatial and temporal resolutions by the Priestley-Taylor Two-Source Energy Balance model (TSEB-PT) driven by Copernicus satellite data. We build an automatic workflow to generate 100-m ET product by combining data from Sentinel-2 (S2) MSI and Sentinel-3 (S3) land surface temperature (LST) with ERA5 climate reanalysis derived within the period 2017-2021 over four Mediterranean basins in Italy, Spain,
15   France, and Tunisia (Po, Ebro, Hérault, Medjerda). First, original S2 data are pre-processed before deriving 100-m inputs for the ET estimation. Next, biophysical variables, like leaf area index, and fractional vegetation cover are generated, and then they are temporally composited within a 10-day window according to Sentinel-3 acquisitions. Consequently, decadal S2 mosaics are used to derive the remaining TSEB inputs. In parallel, we sharpen 1-km S3 by exploiting dependency between coarse-resolution LST and 100-m S2 reflectances using the decision trees algorithm. Afterward, climate forcings are utilized
20   for modeling energy fluxes, and next for daily ET retrieval. The daily ET composites demonstrate reasonable TSEB-PT estimates. Based on the validation results against eight Eddy Covariance (EC) towers between 2017-2021, the model predicts 100-m ET with an average root mean square error of 1.38 mm day^{-1} and Pearson coefficient equal to 0.60. Regardless of some constraints, mostly related to the high complexity of EC sites, TSEB-PT can effectively estimate 100-m ET, which opens up new opportunities for monitoring the hydrological cycle on a regional scale. The full dataset is freely available at
25   https://doi.org/10.48784/b90a02d6-5d13-4acd-b11c-99a0d381ca9a,   https://doi.org/10.48784/fb631817-189f-4b57-af6a-38cef217bad3, https://doi.org/10.48784/70cd192c-0d46-4811-ad1d-51a09734a2e9, and https://doi.org/10.48784/7abdbd94-ddfe-48df-ab09-341ad2f52e47 for Ebro, Hérault, Medjerda, and Po catchments, respectively (Bartkowiak et al., 2023a-d).

1 Introduction

30   Terrestrial evapotranspiration (ET) is a keystone component for estimating water loss from the Earth's surface, being the main indicator of biophysical conditions for vegetation and bare soil (Coenders-Gerrits et al., 2020; Gouveia et al., 2017). Designated as an essential climate variable, ET substantially contributes to hydrological, energy, and carbon cycles through its high sensitivity to atmosphere-land interactions, particularly crucial in the context of a warming climate (Fisher et al., 2017; Konapala et al., 2020). Given its significance, ET finds widespread use in various environmental applications, including

35   climate studies (Chattopadhyay and Hulme, 1997; Dezsi et al., 2018; Gao et al., 2017), drought detection (Maes and Steppe, 2012; Otkin et al., 2016), sustainable agriculture and food production (Allen et al., 1998; Cammalleri et al., 2014; Dari et al., 2022), and also natural ecosystem monitoring (Anderson et al., 2012; Granata et al., 2020). However, most of these activities require spatially continuous ET data with regular revisit time and long-term observation records (Jiang et al., 2021). While conventional *in-situ* measurements such as lysimeters, Eddy Covariance (EC), and Bowen ratio techniques (Allen et al., 1991;

40   Buttar et al., 2008; Pastorello et al., 2020) provide frequent time-series, their limited spatial coverage and sparse network restrict their practical utility compared to gridded ET products.

        Over the past few decades, many methods have been developed for retrieving spatially distributed ET over large areas, which can be categorized into two groups: process-based and data-driven approaches. The first category comprises physical modeling methods that derive energy fluxes based on theoretical assumptions. These approaches rely on various forcing

45   parameters to explain ET and have been proposed by many researchers (Allen et al., 1998; Monteith, 1965; Norman et al., 1995; Penman, 1948; Priestley and Taylor, 1972; Su, 2002; Mallick et al., 2014). In contrast, the second group is based on empirical relationships between ET and its controlling predictors. These relationships are derived from *in-situ* and remotely sensed observations and are mainly established using statistical regressions (Maselli et al., 2014), machine learning (ML) and deep learning (DL) algorithms, like random forest (Douna et al., 2021), artificial neural networks (Ferreira et al., 2019; Jain et

50   al., 2008), and long short-term memory (Babaeian et al., 2022). In these data-driven approaches, the focus is primarily on the statistical patterns and correlations between the observed variables and ET, with minimal incorporation of physical mechanisms into a model. In recent years, to achieve a balance between physical principles and model-learned relationships over large and diverse datasets, the scientific community has proposed process-constrained ML/DL methods that combine data-driven algorithms with process-based modeling (Cui et al., 2021; Hu et al., 2021; Reichstein et al., 2019).

55   Regardless of the ET method employed, open-source global climate datasets, like the European ReAnalysis V5 (ERA5) and NASA Global Land Data Assimilation System (GLDAS), in conjunction with a surge in spaceborne Earth Observation (EO) technologies have greatly accelerated development of many gridded ET products (Bhattarai and Wagle, 2021; García-Santos et al., 2022). Although ET cannot be directly measured from space, since the 1980s EO satellites have been providing valuable observations of the land surface parameters, enabling estimation of actual ET at large scales (Zhang et al., 2016). One

60   notable advantage of freely accessible global ET products is their spatiotemporal continuity and related long-term availability. In recent years, several long-term datasets have been developed, including the GLDAS Catchment Land Surface Model

(CLSM) encompassing the years 1948 to 2014, and the Priestley–Taylor-based Global Land Evaporation Amsterdam Model (GLEAM), covering the period from 1980 to the present (Li et al., 2018; Miralles et al., 2011; Martens et al., 2017). Although these global-scale models provide extensive time-series at the continental level, serving as a valuable parameter for many

65 hydrological models (Alfieri et al., 2022; López López et al., 2017) and offering important insights into water availability at a large scale (Bai and Liu, 2018), they provide ET data at spatial resolutions of tens of kilometres. Since 2015, daily 3-km ET maps, driven by the Spinning Enhanced Visible and InfraRed Imager (SEVIRI) onboard the geostationary Meteosat Second Generation (MSG) satellite, have been generated and made available through the LSA-SAF system (*https://landsaf.ipma.pt/*). Additionally, other global ET products include the Penman–Monteith MOD16 maps driven by MODerate resolution Imaging

70 Spectroradiometer (MODIS) inputs (Mu et al., 2007), and Operational Simplified Surface Energy Balance (SSEBop) ET, typically utilizing the 1-km MODIS LST and Leaf Area Index (LAI) products and climate reanalysis datasets (Senay et al., 2013), among others that have been successfully applied in many regions (Weerasinghe et al., 2020). Despite their reliable validation results in relatively homogenous landscapes, like the contiguous United States (CONUS) with an average R^2 of 0.7 for both SSEBop and MOD16 (Velpuri et al., 2013), their large pixel size and related insensitivity to complex terrain might

75 not be representative over heterogenous locations (Castelli, 2021; McShane et al., 2017).

Surface energy balance (SEB) modeling is a valuable tool for estimating ET using high spatial resolution (HR) thermal remote sensing, like sub-field scale Landsat LST imagery with a pixel size ranging from 60-120 m, and 70-m ECOsystem Spaceborne Thermal Radiometer Experiment (ECOSTRESS) mission launched in 2018 (Anderson et al., 2021; Xue et al., 2022). Currently, the global HR ECOSTRESS ET data is generated from the Priestley-Taylor Jet Propulsion Laboratory (PT-

80 JPL) algorithm (Fisher et al., 2008; Fisher, 2018). To expand the high capabilities of the HR LST, Cawse-Nicholson and Anderson (2021) have introduced the disaggregated Atmosphere-Land Exchange Inverse Jet Propulsion Laboratory (DisALEXI-JPL) model, which provides ECOSTRESS-driven energy fluxes over the CONUS area. Additionally, the ESA European ECOSTRESS Hub data repository has been released that offers an open-source 70-m daily evaporation product for Europe and Africa based on the non-parametric Surface Temperature Initiated Closure (STIC) model (Hu et al., 2022; Mallick

85 et al., 2014). Even though the HR ET datasets obtain satisfactory results, the irregular revisit time of ECOSTRESS over Europe and the 8–16-day repeat cycle for Landsat hamper their use in monitoring ET dynamics and temporal trends. In this regard, next-generations of HR thermal missions are designed, including ESA Copernicus Land Surface Temperature Monitoring (LSTM), Thermal infraRed Imaging Satellite for High-resolution Natural resource Assessment (TRISHNA) of CNES-ISRO (France-India), and NASA Surface Biology and Geology (SGB) TIR. Even though these instruments are planned to be

90 launched between 2024 and 2028, their operational use will be further delayed. Thus, there is an urgent need to bridge this gap by advancing current satellite-based ET estimates.

Given the limited availability of high spatiotemporal LST data, such as those with both daily revisit time and sub-kilometre pixel size, SEB-based retrievals have been commonly enhanced by spatially downscaling daily TIR images obtained from 1-km satellite sensors like Terra/Aqua MODIS, Visible Infrared Imaging Radiometer Suite (VIIRS) onboard Suomi National

95 Polar-orbiting Partnership (S-NPP), and Sentinel-3 Sea and Land Surface Temperature Radiometer (SLSTR) (Bisquert et al.,

2016; Guzinski and Nieto, 2019; Xue et al., 2021). Due to the increasing volume and variability of geospatial data, many data-driven approaches have been proposed, relying on empirical relationships between 1-km surface temperatures and high-resolution explanatory variables derived from Synthetic Aperture Radar (SAR) and Visible Shortwave Infrared (VSWIR) sensors (Li et al., 2019; Mao et al., 2021; Pu and Bonafoni, 2023). For instance, Liu et al. (2020) employed a random forest

100 algorithm to derive 250-m MODIS LSTs over northern China, reporting an improvement in RMSE of 32%-36% compared to the original 1-km images. Furthermore, since 2019 the FAO initiative WaPOR has provided 10-day ET composites over Africa and the Middle East derived from the ETLook model and driven by MODIS, PROBA-V, and Landsat data at continental, country, and subnational scales, corresponding to resolutions of 250-m, 100-m, and 30-m, respectively (Bastiaanssen et al., 2012; Blatchford et al., 2020). In parallel, the Two-Source Energy Balance (TSEB) model, forced by ESA Copernicus data,

105 has demonstrated potential for producing HR ET with global coverage (Bellvert et al., 2020; Guzinski et al., 2020; Chintala et al., 2022). The frequent acquisitions of the HR Sentinel-2 MultiSpectral Instrument (MSI) and 1-km Sentinel-3 SLSTR with the two-satellite configurations, along with global ERA5 climate data, serve as reliable inputs for TSEB due to their long-term continuity and evolution plans. As reported by Guzinski et al. (2021), Copernicus datasets, including downscaled Sentinel-3 LST to resolutions ranging from 20 to 300 m, exhibit better spatial-scale consistency than WaPOR inputs, resulting in a

110 correlation coefficient equal to 0.9 and a mean bias of less than 0.3 mm day^{-1} over Mediterranean agricultural areas in Tunisia and Spain during growing season in 2018-2019.

In this study, we aim to produce Copernicus-based ET maps for the Mediterranean region (MR) utilizing the Two-Source Energy Balance model with a dual-source scheme, which allows estimating energy fluxes for both vegetation and soil components. The ET product covers the years 2017-2021 and is generated at high spatiotemporal resolutions of 100 m on a

115 daily basis as a reasonable scale over a fragmented Mediterranean landscape. The maps are derived using freely available algorithms developed within the ESA Sentinels for Evapotranspiration (Sen-ET) initiative (DHI-GRAS, 2020). In general, we synergistically combine high-resolution Sentinel-2 shortwave data, moderate-resolution Sentinel-3 LST images, and ERA5 climate observations to generate the ET grids. Due to big data volume and the multi-step processing involved, the objective of this study is also to automatize the entire workflow for large-scale applications and provide recommendations for facilitating

120 Sen-ET inputs and algorithms through cloud computing infrastructure. To achieve this, we implement the entire workflow using cloud computing units offered by VMware, EODC, and CloudFerro. The processing pipelines are designed to update the resulting ET time-series and make it more suitable for operational use. To the best of our knowledge, it is the first application of the TSEB at sub-kilometre spatial resolution over the Mediterranean Basin. Notably, such areas are often underrepresented in global-oriented studies, making this work particularly useful in advancing our understanding of ET in

125 regions of both high ecohydrological and socio-economic importance.

2 Study area and datasets

2.1 Study sites

Our study focuses on four Mediterranean river basins: Ebro in Spain, Po in Italy, Medjerda in Tunisia, and the French Languedoc-Roussillon with the Hérault basin. The regions cover a total area of approximately 190 000 km². Figure 1 depicts
130 the geographical locations of all areas of interest.

(a)

(b)   **(c)**   **(d)**   **(e)**
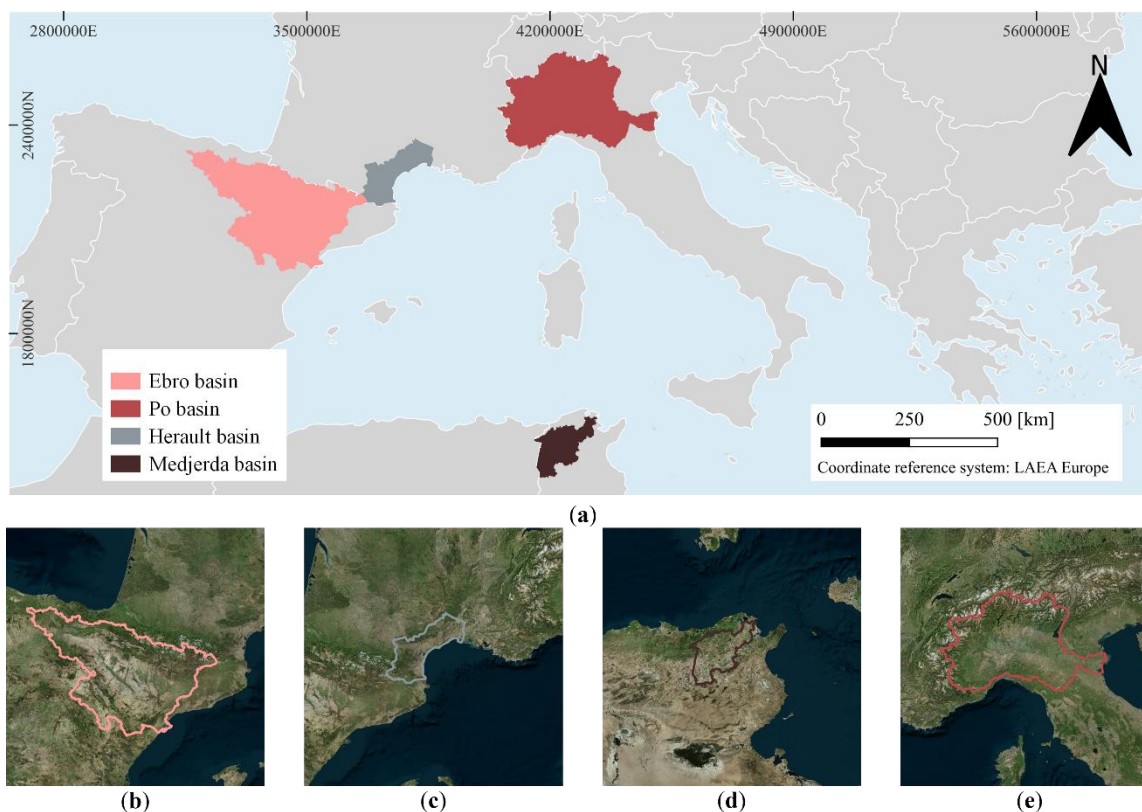
Figure 1: Overview of the areas of interest: (a) general location of the basins in the Mediterranean region; (b)-(e) Ebro, Hérault, Medjerda, Po basins. All figures were generated in QGIS using internal resources (Figure 1a) and open-source layers provided by *https://www.bing.com/maps* **(Figures 1b-e) © Microsoft.**

As demonstrated in Fig.1, the Ebro basin (EB), with a total catchment size of about 85 500 km², exhibits a diverse
135 landscape, leading to varied climatic conditions. The EB experiences an oceanic and Mediterranean mountain climate in the north with an average annual air temperature (TA$_{mean}$) ranging from 9°C to 12°C. Moving southeast, the climate transitions into a warm oceanic climate, where TA$_{mean}$ ranges from 11 to 14°C (Lorenzo-González et al., 2023). Precipitation patterns also vary across the region. The south-eastern part experiences low precipitation (350–700 mm yr^{-1}), while the mountain regions receive more rainfall yielding 800-2000 mm per year (Gaona et al., 2022). To meet the water demands of the entire EB,
140 extensive canal systems have been developed, and around 92% of the total water consumption is allocated to irrigation and farming (Barella-Ortiz et al., 2023). Similarly, in the Po basin (PB), which spans an approximate surface area of 71 000 km²,

the climate and water resources are strongly influenced by the region topography. The northern PB is known for its Alpine climate, and it is characterized by numerous water reservoirs commonly used for energy generation. The southern areas, despite having a lower water supply, play a vital role in agriculture due to their large water storage capacities and favourable terrain

145   (Dari et al., 2023). TA_{mean} in the Po basin varies across the region. In the mountains, TA_{mean} ranges from 5 to 10°C, while in the remaining zones it falls within the range of 10 to 15°C (Musolino et al., 2017). Additionally, the average precipitation ranges between 700 and 1500 mm per year (Filippucci et al., 2022). The coastal Languedoc-Roussillon (LR) region in southern France represents another agriculture-oriented basin, with nearly 30% of arable land represented by vineyards (Cambrea et al., 2020). The LR is primarily influenced by a Mediterranean climate characterized by hot, dry summers and mild winters. The

150   southern sections of the Pyrenees exhibit nival climatic conditions. Similar to the EB and PB, the Hérault basin follows a climatic gradient that is dependent on its geolocation. In the northern part, the yearly TAs_{mean} ranges around 8°C, while precipitation reaches 1600 mm per year. In contrast, the southern part experiences higher temperatures, with TA_{mean} surpassing 15°C, and lower rainfall levels of around 600 mm yr^{-1} (Fabre et al., 2015). The Medjerda basin (MB) in Tunisia represents a catchment with drier and hotter climatic conditions compared to the other study sites. In fact, it is characterized by low annual

155   precipitation varying between 350 mm and 600 mm, coupled with high annual temperatures averaging between 16 and 22°C (Rajosoa et al., 2022). With an area of approximately 15 500 km^2, the MB is the largest watershed in Tunisia, and thus it holds significant importance in terms of water supply for both domestic use and farming (Boulmaiz et al., 2022). Indeed, agriculture plays a dominant role, consuming the largest amount of water resources, accounting for nearly 76% of the total water volume available (FAO, 2020).

160   Given the hydro-demanding activities across the study sites, which include crop irrigation, energy production, mass tourism, as well as domestic water use, and on the other side the challenges posed by extreme heatwaves and recurring droughts in recent years, daily ET maps at the river basin scale would be highly beneficial for supporting vegetation monitoring and sustainable water management practices (Gouveia et al., 2017).

2.2 In-situ measurements

165   In this study, Eddy Covariance (EC) measurements collected in the framework of the European Fluxes Database Cluster (EFDC) are used to validate gridded ET products (Heiskanen et al., 2022). EFDC is the European initiative that gathers and standardizes *in-situ* fluxes from a wide range of the EC networks (e.g., ICOS, InGOS, CarboItaly, and GHG-Europe) to facilitate their application among the scientific community worldwide. The database stores long-term measurements (since 1996) that are pre-processed and quality-controlled by providers before data submission to the system.

170   In this work, after deriving all measurements from the EFDC, all available EC records have been harmonized and made available as a multi-year file stack with daily time step through the project-dedicated PostgreSQL database (*https://edp-portal.eurac.edu/*). Consequently, ground-based EC data are analysed for eight stations located in the study subdomains (see Sect. 2.1 for more details). The sites are represented by different vegetated land covers which include alpine grasslands, forest, and vineyard ecosystems. As depicted in Table 1, five towers are located in mountain regions above 1400 m a.s.l. and are

175 covered by grasslands and forest, while three remaining towers lie in forest and vineyard biomes in France and Italy at altitudes
ranging from 1 to 270 m a.s.l. Considering the time span of the generated ET product, *in-situ* measurements temporally overlap
with Copernicus Sentinel-3 LST data acquired between 2017 and 2021.

Table 1: Eddy Covariance stations for validating gridded ET maps.

Station name	EC site ID	Landcover	Elevation	Data availability*
Puéchabon	FR-Pue	EBF	270 m	2000-2021
Lison	IT-Lsn	VIN	1 m	2016-2020
Muntatschinig meadow	IT-MtM	GRA	1450 m	2017-2019
Muntatschinig pasture	IT-MtP	GRA	1550 m	2017
Torgnon	IT-Tor	GRA	2160 m	2008-2020
Renon	IT-Ren	ENF	1730 m	1999-2020
San Rossore 2	IT-SR2	ENF	4 m	2013-2020
Monte Bondone	IT-MBo	GRA	1550 m	2003-2020

*time span for raw local measurements before excluding years of non-interest
180 EBF = evergreen broadleaf forest, VIN = vineyard, GRA = grassland, ENF = evergreen needleleaf forest

To derive daily ET observations with good quality, all *in-situ* latent heat flux (LE) measurements were first pre-processed
to eliminate outliers, duplicates, rainy events (> 0 mm day^{-1}), and eventually days with a sub-daily coverage smaller than 25%.
Additionally, station records with low-quality assurance (QA) are removed. In case of missing QA flags, we exclude the
corresponding data records from further analysis. As a result, the amount of ground measurements is reduced. After the quality
185 checks, the local ET observations are estimated using the approach proposed by *Allen et al.* (1998). Specifically, latent heat
flux [W m^{-2}] is converted to daily ET [mm day^{-1}] using the following formula:

$$ET \left[\frac{mm}{day}\right] = \frac{LE\left[\frac{W}{m^2}\right] \times 24 \times 60 \times 60 \left[\frac{s}{day}\right] \times 1000 \left[\frac{mm}{m}\right]}{\rho_w\left[\frac{kg}{m^3}\right] \times L\left[\frac{J}{kg}\right]}, \tag{1}$$

where ρ_w is the water density (1000 kg m^{-3}), and L represents the latent heat of vaporization (2.25·10^6 J kg^{-1}). After the equation
transformation, the tower-derived ET is estimated, and then compared against the 100-m ET product as described in the next
190 sections of this paper.

2.3 Gridded data

Multi-source ESA Copernicus data to estimate actual ET are used in this study: satellite, meteorological, and ancillary
remotely sensed variables. This chapter outlines source datasets and the accompanying preprocessing steps involved before
the main processing chain for deriving ET. Table 2 provides a comprehensive overview of all gridded variables utilized for
195 the ET modeling. It should be mentioned that in Sect. 3 we present more details on all Copernicus-based outputs at intermediate
and final processing stages with cloud computing resources.

Table 2: Gridded data used in this study.

Source dataset	Input parameter	Pixel size	Brief summary
Sentinel-3A/B Sea and Land Surface Temperature Radiometer (SLSTR) Level 2	Land surface temperature (LST)	1 km	LST maps at clear-sky conditions based on quality bands provided (ESA, 2022) and downscaled to 100-m spatial resolution
Sentinel-2A/B Multispectral Instrument (MSI) Level 1C and 2A	Surface reflectance (SR)	10-20 m	Top-Of-Atmosphere (Level-1C) and the Bottom-Of-Atmosphere (Level 2A) SR bands resampled to 100-m and 1-km pixel size*
Shuttle Radar Topography Mission (SRTM)	Elevation (DEM)	90 m	Digital elevation model (DEM) from the SRTM and its two derivatives: slope and aspect resampled to 100 m and 1 km spatial resolution*
PROBA-V and Sentinel-3 Ocean and Land Colour Instrument (OLCI)	Landcover	300 m	Annual maps with global extent derived from PROBA-V (2017-2019) and Sentinel-3 OLCI for the years 2020-2021 resampled to 100 m pixel size
European ReAnalysis V5 (ERA5)	Meteorological data	31 km	Hourly maps of air temperature, vapor pressure, air pressure, wind speed, clear-sky downward solar radiation, and daily all sky downwelling shortwave flux, all matched to Sentinel-3 overpass time

*both 1-km and 100-m datasets are utilized for data-driven thermal downscaling, while 100-m intermediate outputs are incorporated directly into the ET model

In this work, the ET model is forced by Copernicus satellite data, including daily 1-km Sentinel-3 LST maps and fine spatio-temporal resolution Sentinel-2 MSI imagery (10-20-m, 2-5 days revisit time), all derived for the years 2017-2021. Land surface temperature, as a crucial forcing parameter for the ET model, corresponds to daytime S3 acquisitions under clear-sky conditions. Simultaneously, biophysical variables and shortwave bands at 100-m resolution are derived from original S2 L2A reflectance maps with a total spatial coverage of 52 Sentinel-2 tiles (Table 2). In case of missing Sentinel-2 at the Bottom-Of-Atmosphere (S2L2A), we first pre-process Sentinel-2 Level-1C (S2L1C) to derive atmospherically corrected S2 scenes, as explained in the next sections of this paper. In this work, daytime land surface temperature images, as a crucial forcing parameter for estimating turbulent fluxes, are derived from Sentinel-3A and Sentinel-3B SLSTR data. In this regard, we extract specific bands from 1-km S3 products, including LST, and cloud mask, along with sun and S3 sensor geometries. Due to the two-satellite constellation since June 2018, Sentinel-3 acquisitions with minimum viewing zenith angle (VZA) are selected when multiple scenes on the same day are captured. The reason behind that choice is motivated by the fact that larger VZA has a more negative impact on surface temperature accuracy due to angular anisotropy in the thermal infrared spectrum. To derive surface biophysical variables for ET modeling, the constellation of Sentinel-2 MSI (both A and B) is exploited, and in particular, 10-20 m nine reflectance bands from the Visible ShortWave InfraRed (VSWIR) region are extracted. In addition, the resulting S2 L2A shortwave channels are used as 100-m predictor variables to downscale 1-km Sentinel-3 SLSTR LST data. More details on satellite data preparation are in the next sections of this paper.

To run the ET processing chain, other two satellite-driven products are also exploited: 300-m Copernicus Climate Change Initiative (CCI) land-cover (LC) maps (*https://www.esa-landcover-cci.org/*) and elevation data obtained from 90-m Shuttle

Radar Topography Mission (SRTM). The first one is derived through the Climate Data Store (CDS) API client in Python as explained at *https://cds.climate.copernicus.eu/*, while DEM is automatically downloaded from the SRTM-dedicated database
220 available online (*https://srtm.csi.cgiar.org*). After data downloading both inputs are resampled to 100-m resolution to be ready for ET model runs. Despite the pixel size discrepancy between inputs and the ET product, this choice is reasoned by temporal coverage of the CCI LS data (2017-2021) with specially designed look-up tables for estimating ancillary parameters to force TSEB model, such as canopy height, fractional vegetation cover, average leaf size, and canopy shape. In case of elevation, we select a 90-m SRTM DEM product due to its ET-like spatial resolution. Apart from that, DEM information is used as an input
225 predictor for downscaling 1-km Sentinel-3 LST, and to topographically correct ERA5 parameters.

Meteorological parameters, which are essential input variables for ET estimation, are derived from high-frequency European ReAnalysis V5 (ERA5) climate data provided by the European Centre for Medium-Range Weather Forecasts (ECMWF) and downloaded from the CDS for the period 2017-2021 (Hersbach et al., 2020). As forcing inputs for the TSEB model, we use meteorological observations that include air temperature (TA), vapor pressure (VP), wind speed (both u and v
230 components), surface pressure (SP), together with two ERA5 solar radiation components: all-sky shortwave downwelling fluxes and clear-sky downward shortwave radiation ($SW_{in}^{clear-sky}$) temporally matched to Sentinel-3 SLSTR overpass time. Hourly $SW_{in}^{clear-sky}$ datasets are selected rather than all-sky downwelling solar irradiance due to an assumption of clear-sky conditions during S3 acquisitions incapable of penetrating clouds. ERA5 dataset is used for estimating input parameters, like net shortwave radiation and longwave irradiance, and then for deriving instantaneous energy fluxes and extrapolating latent
235 heat flux to daily time steps.

3 Methodology

3.1 General framework

This study aims to develop an automatic workflow for generating Copernicus-based daily ET datasets at 100-m resolution from 2017 to 2021. Sub-kilometre ET mapping is considered a reasonable scale in the Mediterranean region characterized by
240 complex topography and highly patched landcover, where 1-km ET maps might not fully represent spatial heterogeneities of the land surface (Massari et al., 2021). In general, the entire workflow to produce a daily 100-m ET product consists of two steps: (1) input parameter preparation, and (2) TSEB modeling of ET (Figure 2). In the following subchapters we describe each processing chain in more detail.
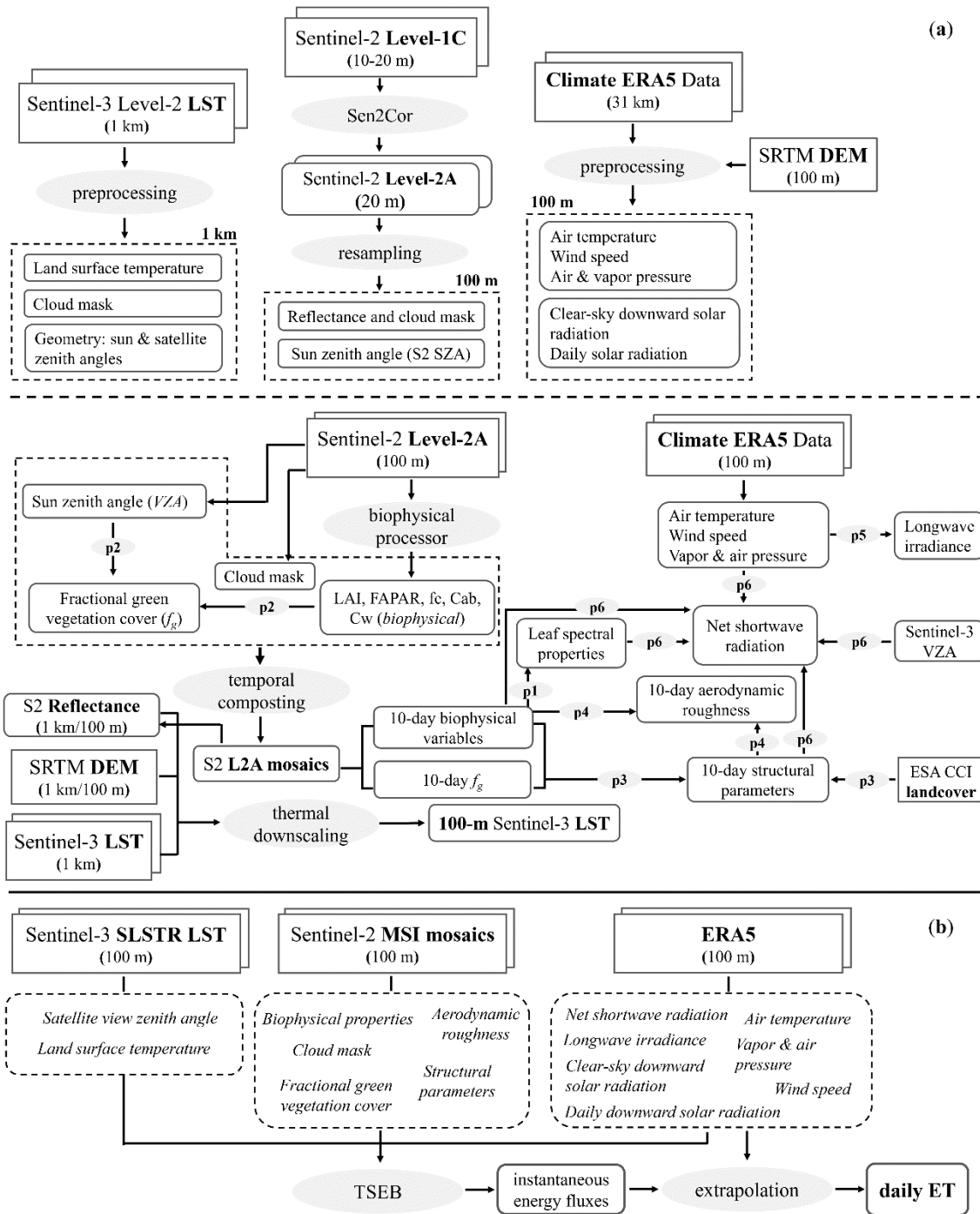
Figure 2: Schematic flowchart of the entire ET processing including (a) source data preprocessing (the top row) and input retrievals
245 **for Two-source Energy Balance (TSEB) modeling (the lower line), (b) daily ET estimation at 100 m resolution. While processes are**
represented by ovals (e.g., preprocessing, thermal downscaling, TSEB modeling, and intermediate p1-p6), rectangles stand for
source parameters, and round rectangles indicate intermediate and final results.

Owing to the large-scale ET modeling and its related high computational and memory requirements, we distribute our work on multiple virtual machines. We implement the processing flow with the setup on Ubuntu v20.04 LTS using two geospatial cloud computing platforms offered by EODC (*https://eodc.eu/*) and ESA High-Performance Computing (HPC) cluster of CloudFerro (*https://cloudferro.com/*). The main advantage of this solution is the direct access to satellite data and the capability to facilitate big data processing more robustly. Apart from these resources, two internal units of EURAC Research with Ubuntu v18.04 LTS are deployed on VMware machines (*https://www.vmware.com/*). In this case, EO data are directly downloaded from the ESA Copernicus Open Access Hub (*https://scihub.copernicus.eu/*). The multiple selection of cloud providers is motivated by two reasons. First, the entire procedure for deriving ET maps at 100-m resolution is complex (see Figure 2), which translates to big requirements in terms of disk space, computing memory, and processing time. For example, a five-year dataset (2017-2021), including intermediate and final outputs over one Sentinel-2 tile requires around 600 GB. Secondly, we diversify our processing workflows into many computing units due to their accessibility offered by the ESA Network of Resources (NoR) sponsorship program. Furthermore, in the framework of the 4DMed-Hydrology project EURAC Research was requested to test the new ESA HPC infrastructure considering the high-volume processing of the entire workflow presented in this study.

To keep the data pipeline consistent over the multiple platforms, we harmonize the entire workflow by creating a unique Conda environment on all our machines. ET outputs are obtained by automatizing entire routines, including baseline ESA SNAP Graphical Processing Tool (GPT) algorithms and Python baseline codes developed in the framework of Sen-ET project (*https://www.esa-sen4et.org*). For more specific details on the data (pre)processing for both satellite and meteorological parameters, it is recommended to visit the open-source GitHub repository available at *https://github.com/DHI-GRAS/*. The repository includes codes that calculate necessary inputs for the TSEB model.

3.2 Input parameter preparation

Considering multi-source datasets in conjunction with their different processing levels and spatial scales, the primary step of our workflow includes source data preprocessing, and input preparation for forcing the Two-Source Energy Balance (TSEB) model (Table 2, Figure 2a).

First, we spatially aggregate 20-m Sentinel-2 Level 2A reflectances and their geometries to 100-m pixel size with an arithmetic mean function. In this study, we select 100-m resolution for the ET product rather than the original 20-m S2 cell size. Prior to final modeling we tested the impact of spatial resolution of input variables on the final ET estimates considering the abovementioned pixel dimensions. ET simulations forced by 20-m and 100-m parameters gave similar results, and thus the latter solution was chosen as a trade-off between high spatial resolution and storage use along with computing speed. In addition, to our best knowledge, long-term high-resolution ancillary variables, e.g., elevation and landcover at spatial resolution < 100 m are not freely available to be incorporated into the entire workflow.

Nevertheless, S2 L2A preparation is challenging mainly due to incomplete timeseries on the EODC service. This requires copying missing datasets either from CloudFerro or from the Copernicus Open Access Hub. Apart from that, Sentinel-2 data

over Medjerda basin in Africa between 2017 and mid-2018 are not available on all platforms (last accessed on 9 January 2022). As shown in Figure 2a, in that case Sentinel-2 Level 1C (S2 L1C) scenes are first pre-processed with Sen2Cor processor to obtain atmospherically corrected 20-m S2 L2A granules together with a scene classification layer for cloud removal afterwards (Main-Knorn et al., 2017). Since the time frame of this work covers the years 2017-2021, it is necessary to use two different

285 versions of Sen2Cor. Indeed, Sen2Cor 2.5.5 is able to ingest only those data belonging to 2017-2021; while S2 scenes from 2022 need to be processed using the Sen2Cor 2.10.01. To solve this problem, we setup two different docker containers for the two Sen2Cor versions. After checking the acquisition date of the input data, the bash script is run considering the time overlapping Sen2Cor releases. Due to straight-forward Sen2Cor cloud mask retrieval and its well-established workflow, we decided to apply this approach for the entire Sentinel-2 time-series.

290 Next, S2-driven biophysical parameters, including leaf area index (LAI), canopy height (h_C), and fractional vegetation cover (f_C), are produced using the S2 Toolbox Biophysical processor (Weiss and Baret, 2016; Xie et al., 2019). The entire procedure requires eight Sentinel-2 L2A bands acquired in the VSWIR electromagnetic spectrum together with geometry information, like sun and sensor zenith angle. LAI retrieval is a hybrid approach based on an inversion of the PROSAIL radiative transfer model simulations of S2 canopy reflectance using neural network modeling. More details on estimating

295 biophysical variables are provided by *Weiss and Baret* (2016). At the same time, the fraction of green vegetation (f_g) is generated by incorporating the S2 VZA and biophysical variables as input parameters (Figure 2b). To minimize the cloud cover effect in Sentinel-2 product, all the abovementioned outputs are mosaicked using a 10-day window with respect to Sentinel-3 overpass dates. This means that time coincident Sentinel-2 granules are temporally ranked and good quality pixels with possibly the closest date to S3 acquisition are selected. The entire procedure is developed in SNAP GPT to be run in an

300 automated manner over the entire image collection. Next, 10-day composites are utilized in conjunction with other ET model parameters, like 100-m CCI landcover, for deriving remaining inputs, including aerodynamic roughness, along with vegetation structural and spectral properties as shown in Figure 2b. In addition, atmospherically corrected surface reflectance (SR) bands are resampled to 1 km spatial resolution to sharpen Sentinel-3 LST data.

As outlined in Sect. 2.3, we use satellite-based land surface temperature from 1-km Sentinel-3 SLSTR Level-2 data for

305 estimating actual ET. Given the sensitivity of TIR instruments to overcast conditions, all cloudy pixels are eliminated with respect to the *cloud-in* mask provided with SL_2_LST product. Next, S3 datasets are cropped according to Sentinel-2 tiles (*https://sentinels.copernicus.eu/web/sentinel/missions/sentinel-2/data-products*) and reprojected to the WGS84 coordinate system for their synergistic use with Sentinel-2 data afterwards.

Notably, it should be mentioned that CloudFerro provides different versions of Sentinel-3 LST in terms of cropping scheme,

310 baseline collections, and related software versions for data processing. This hinders the immediate use of the data and requires an investment of time to analyze the quality of the data and choose the proper version, and thus S3 LST processing needs to be preceded by data checks and proper filtering. In general, it is recommended that the newest baseline collection (v4) is chosen rather than a product with baseline collection v3 as the v4 is reprocessed using an upgraded software after major evolutions.

While taking advantage of complementary Sentinel-2 and Sentinel-3 instruments, we sharpen 1-km S3 SL_2_LST product
315   to derive enhanced surface temperatures at a spatial resolution corresponding to our ET product (Figure 2a). Thermal
downscaling is based on the Data Mining Sharpener (DMS) approach proposed by *Gao et al.* (2012). It has been successfully
applied in many studies to enhance the spatial consistency of LST grids (Anderson et al., 2021; Guzinski et al., 2020). The
kernel-driven regressions are obtained from the bagging ensemble of decision trees (DT) algorithm that reduces the risk of
model overfitting. In this study, DMS predicts land surface temperature at 100 m spatial resolution by exploiting empirical
320   relationships between coarse LST grids and high-resolution explanatory variables for each Sentinel-3 acquisition date. The
functional relationship between clear-sky Sentinel-3 LST data and explanatory variables is based on 10-day S2 reflectance
composites in conjunction with DEM and shortwave irradiance incident angle at S3 overpass time derived from SRTM-based
slope, and aspect grids (Figure 2b). DMS method establishes simultaneously global (within 100-km S2 tile) and local (30 by
30 Sentinel-3 pixels within a moving window) regression models, and then fuses these two estimates as their weighted linear
325   combination to increase the number of samples for model training, and also captures thermal heterogeneity at local scale.
Consequently, downscaled LST maps are derived by applying daily models to the HR predictors, while forcing energy
conservation between original Sentinel-3 images and sharpened granules. The entire procedure is performed in the blending
phase by applying a weight to global and local estimates based on residual correction between the original LST and the 100-
m S3 image sharpened with two regression schemes. This means that LST pixels with lower bias result in bigger weight, while
330   grid cells with larger residuals have a smaller impact on the final LST estimation.

Given a wide range of fine resolution predictors (< 100 m) and their high revisit time (2-5 days), the enhancement method
in the spatial domain is selected rather than the image fusion approach that increases temporal availability of high spatial
resolution LST images by exploiting (sub)daily observations from coarse resolution TIR scanners (Sun et al., 2017; Yang et
al., 2017). As mentioned before, the DMS method belongs to well-established downscaling approaches and its recent open-
335   source implementation increases its visibility among users (Guzinski and Nieto, 2019).

ECMWF ERA5 climate datasets also require preprocessing prior to inclusion in the Two-Source Energy Balance model.
All extracted variables from the reanalysis dataset (see Sect. 2.3 for more details), except for wind speed, are corrected for
terrain using the SRTM DEM product (Figure 2a). Similar to instantaneous variables, all-sky shortwave downwelling fluxes
are first enhanced by including topography orientation and an hourly cloud cover factor derived from $SW_{in}^{clear-sky}$, and then
340   interpolated to daily observations. Considering better representativeness of low-resolution meteorological parameters at the
blending height of 100 m rather than 2 m above ground, TA, VP along with SP are additionally recalculated at that height
(Guzinski et al., 2021). Daily average solar radiation is obtained by interpolating hourly ERA5 shortwave downward irradiance
over a 24-hour period starting at midnight local time. Next, the product is used to extrapolate instantaneous latent flux to daily
ET. After calibrating ERA5 components, we prepare specific radiative fluxes for deriving instantaneous energy fluxes
345   corresponding to Sentinel-3 overpass. In this regard, meteorological input is utilized to compute longwave irradiance, and then
instantaneous net shortwave radiation is derived from Sentinel-3 VZA imagery and 10-day Sentinel-2 composites of structural
and biophysical parameters (Figure 2a).

3.3 TSEB modeling of ET

In this work, we utilize the Priestley-Taylor Two-Source Energy Balance model (TSEB-PT) driven by ESA Copernicus
350   data (Figure 2) to produce daily evaporation maps over the Mediterranean region (Norman et al. 1995, Kustas and Norman,
1999). The main advantage of the model over heterogenous areas is the fact that TSEB-PT considers the soil (S) and canopy
(C) as two distinct components and employs a two-layer approach to estimate latent (LE) and sensible heat (H) fluxes for each
element separately:

$$Rn_S = LE_S + H_S + G, \tag{2}$$

355   $$Rn_C = LE_C + H_C, \tag{3}$$

where Rn denotes the net radiation [W m^{-2}], LE represents the latent heat flux [W m^{-2}], H represents the sensible heat flux [W
m^{-2}], and G stands for soil heat flux [W m^{-2}]. Unlike other satellite-based methods, the model minimizes the number of input
parameters, and its relative simplicity makes it an ideal candidate for high-volume processing (Kustas and Anderson, 2009).
The net radiation sub-components (Rn_S and Rn_C) are calculated following the methodology presented by Campbell and
360   Norman in 1998. The H_S (H_C) is determined by evaluating the temperature gradient between the soil (canopy) and the air
temperature (TA) at a reference height, as described by *Guzinski et al.* (2020). The primary remotely sensed variables required
by the model are land surface temperature, which represents the combined effect of both soil and canopy, and fractional
vegetation cover (f_C), used for partitioning the energy between vegetation cover and soil. As the surface temperatures of soil
(LST_S) and vegetation (LST_C) are unknown, TSEB-PT divides LST into soil and canopy temperatures based on the fractional
365   vegetation content, which is parametrized by leaf area index (Guzinski et al., 2014):

$$LST = (f_C LST_C^4 + (1 - f_C) LST_S^4)^{0.25}, \tag{4}$$

TSEB-PT employs an iterative procedure to calculate LST_S and LST_C, along with their respective soil (canopy) sensible heat
fluxes H_S (H_C). The entire process of determining LST_S, H_S, LST_C, and H_C commences with an initial estimation of canopy
transpiration (LE_C^{int}) based on the Priestley-Taylor coefficient α_{PT} (Priestley and Taylor, 1972):

370   $$LE_C^{int} = \alpha_{PT} f_g Rn_C \frac{\Delta}{\Delta + \gamma}, \tag{5}$$

where Δ is the slope of the vapor pressure versus air temperature, and γ is the psychometric constant [kPa K^{-1}]. Having initial
LE_C^{int}, the sensible heat flux from vegetation is calculated as the residual term of the energy balance (Equation 3).
Consequently, LST_C is obtained from the estimated H_C and air temperature as explained in *Nieto et al.* (2019). Next, LST_S is
obtained using Equation (4), and subsequently, the soil sensible heat flux is derived. Finally, LE_S is determined as the residual
375   flux from Equation (2), which ensures energy balance closure. The resistance term is formulated following the approach
proposed by *Kustas and Norman* in 1999. The entire iterative process to derive turbulent fluxes terminates when the soil latent
heat flux reaches a non-negative value. If the obtained LE_C^{int} does not yield a physically realistic solution, the α_{PT} (with an

initial value of 1.26) is successively modified by decreasing it until a physically realistic solution is obtained (Norman et al., 1995; Kustas and Norman, 1999). More details on TSEB may be found in many research studies (Chintala et al., 2022;
380 Guzinski et al., 2020; Hoffmann et al., 2016; Nieto et al., 2019) and open-source Github repository written in Python at *https://github.com/hectornieto/pyTSEB*.

In this study, the TSEB model is forced with gridded inputs, including Sentinel products in conjunction with ERA5 climate parameters for deriving 100-m instantaneous energy fluxes corresponding to Sentinel-3 overpass. As shown in Figure 2b, radiometric temperature and its viewing zenith angle are sourced from the S3 LST product, while biophysical input parameters,
385 like chlorophyll- and water-based leaf reflectance and transmittance, f_C and its green component f_g, are derived from 10-day Sentinel-2 mosaics (see Sect. 3.2 for more detail). While vegetation structural parameters, including leaf angle distribution together with canopy width-to-height ratio variables, are used to compute the clumping index for quantifying foliage distribution, aerodynamic roughness length and zero-plane displacement height serve as inputs for parametrizing resistances required by the TSEP-PT. As summarized in Figure 2b, apart from S3 LST and S2 SR-driven variables, hourly ERA5
390 derivatives are utilized. In this regard, meteorological observations, which include air temperature, wind speed, vapor, and air pressure, are interpolated on a 30-min time scale fitted to Sentinel-3 acquisitions, and then applied to the model. Furthermore, longwave irradiance and net shortwave radiation are incorporated into TSEB for estimating the energy exchange between the surface and the atmosphere. After energy fluxes are obtained (e.g., LE, H, Rn, and G), total latent heat flux is extrapolated to daily ET estimates over each S2 tile using the all-sky ERA5 daily solar irradiance. The last step of the processing flow involves
395 the generation of daily ET maps for our subdomains that include Po, Ebro, Hérault, and Medjerda basins. This is achieved by average mosaicking spatiotemporally tiles using a specially developed composting algorithm as described in Sect. 4 of this paper.

3.4 ET validation

To access the quality of daily ET product, we validate our results using local measurements collected by Eddy Covariance
400 systems (Pastorello et al., 2020). In this regard, we perform ground-based validation by exploiting relationships between *in-situ* daily latent heat fluxes and TSEB-ET estimates. As mentioned in Sect. 2.2, before the validation, LE values are converted to ET estimates expressed in millimetres per day (Allen et al., 1998), and then the resulting datasets are spatiotemporally matched to the 5-year ET dataset (2017-2021). Validation of gridded TSEB outputs requires information on the spatial range of EC towers. Due to parameter-demanding methods for estimating two-dimensional flux footprints, such as the Flux Footprint
405 Prediction climatology proposed by *Kljun et al.* (2015), two simplified validation strategies are chosen: pixelwise and buffer strategies within 100-m cell grid and 50-m radius, respectively. While the first approach is based on the direct extraction of pixel values to points, for the latter method satellite-based TSEB simulations are derived within a 50-m extent around each EC site considering the percentage contribution of each overlapping 100-m pixel in that zone. TSEB validation is performed when ET data cover at least 50% of the total buffer area. In this work, the discrepancies between modelled and observed ET values

410 are evaluated by means of statistical accuracy metrics that include the Root Mean Square Error (RMSE), Pearson correlation coefficient (R), and mean bias (MB). They are calculated as follows:

$$RMSE = \sqrt{\frac{\sum_{i=1}^{n}(x_i - y_i)^2}{n}}; \quad R = \frac{\sum_{i=1}^{n}(x_i - x_{mean})(y_i - y_{mean})}{\sqrt{\sum_{i=1}^{n}(x_i - x_{mean})^2 \sum_{i=1}^{n}(y_i - y_{mean})^2}}; \quad MB = \frac{\sum_{i=1}^{n}(y_i - x_i)}{n}, \tag{6}$$

where x_i stands for the ground-based value on the day i, y_i denotes the predicted value from the TSEB-PT model for a daily observation i, and n is the number of matching observations incorporated in the validation process.

4 Results and discussion

4.1 Evaluation of daily ET at the EC sites

The performance of the ET maps is evaluated against *in-situ* ET data derived from the EFDC database over grasslands (IT-MBo, IT-MtM, IT-MtP, IT-Tor), forest (FR-Pue, IT-Ren, IT-SR2), and vineyard at Lison site (IT-Lsn). First, we examine overall relationships between local ET and TSEB-based estimates under clear-sky conditions together for all sites (Figure 3a).

420 As illustrated in the global scatterplot, the linear regression analysis over all the sites with pixelwise (buffer) approach generates on average RMSE and R of 1.38 mm day^{-1} (1.39 mm day^{-1}) and 0.60 (0.59), respectively. Due to insignificant differences between the two validation strategies applied, in the further part of this study, we focus on the point-based approach.

Note that even though half of the EC towers cover the 4 years between 2017 and 2020 as shown in Table 2, data filtering and its related quality checks together with the necessity to match *in-situ* points with gridded ET values result in a lower number

425 of paired observations for the validation (Table 2, Figure 3).
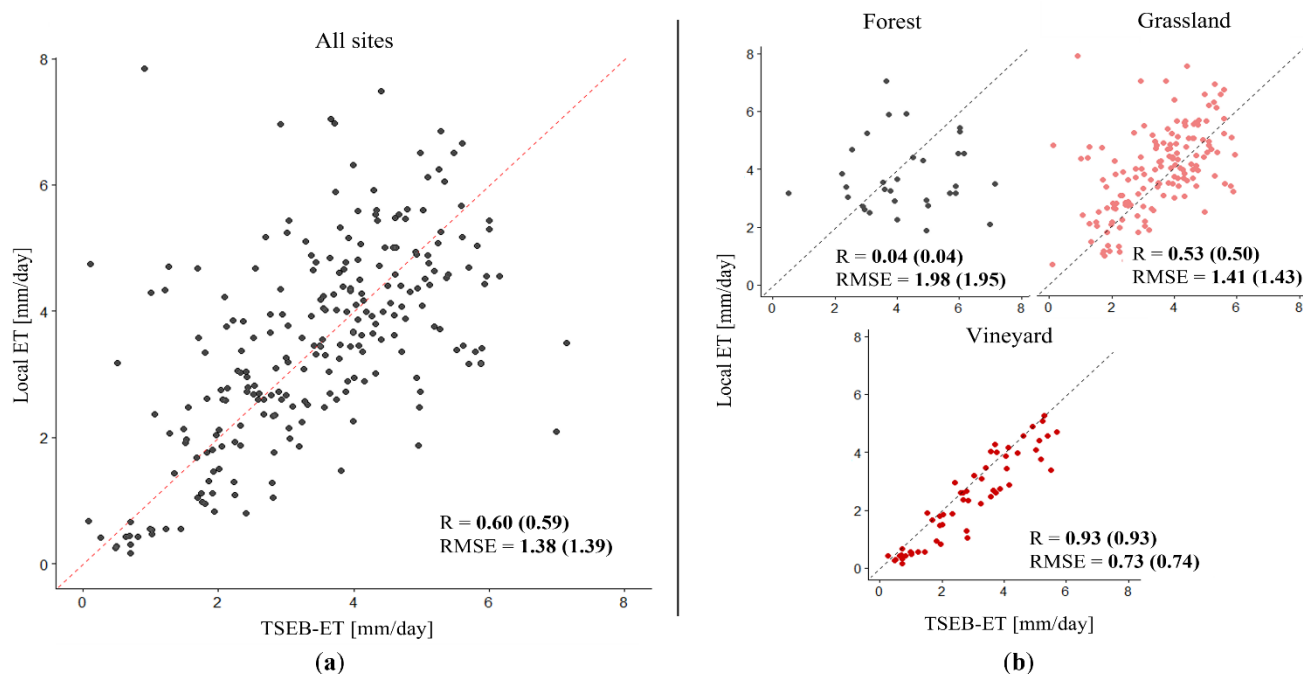
Figure 3: Scatterplots between ground-derived ET observations and TSEB-ET simulations for: (a) all Eddy Covariance sites included, (b) separated landcovers: forest grassland, and vineyard. Note that values in brackets indicate accuracy statistics obtained within 50-m buffer, while records without parentheses represent pixelwise validation strategy.

Second, we investigate TSEB-PT performance considering separately three vegetation biomes, i.e., forest, grasslands, and

430 vineyards. As shown in Figure 3b, the accuracies differ between the landcovers with the best results for lowland vineyards in IT-Lsn yielding RMSE of 0.73 mm per day, and a high score for Pearson coefficient exceeding 0.90. Meanwhile, for grasslands, we observe a moderate correlation between *in-situ* and modelled ET with R = 0.53 and a larger mean error of around 1.41 mm day^{-1} (Figure 3b). Notably, it should be mentioned that all grass-covered EC locations are situated over the Alpine region at altitudes ranging from 1450 to 2160 m a.s.l characterized by relatively steep slopes and high landcover

435 variability (see Appendix A). These factors together with low-resolution inputs like downward and net solar radiation might affect the TSEB-PT performance at the Muntatschinig (IT-MtM and IT-MtP) and IT-Tor sites (Table 3). On the other hand, despite the alpine location of (IT-MBo, the TSEB-PT exhibits a larger potential for estimating daily ET as presented in Table 3. The evaluation metrics for this station indicate a slight underestimation of the model (MB = -0.16 mm day^{-1}) yielding RMSE and R of around 1 mm day^{-1} and 0.7, respectively. The better accuracy statistics over IT-MBo compared to other grass-covered

440 sites are attributable to the relatively homogenous land cover and flat terrain at IT-MBo. The distribution of solar radiation, wind speed, and air temperature gradients are less influenced by a landscape complexity over mountain plateau than over steep slopes, and thus coarse resolution ERA5 might be more representative for IT-MBo compared to IT-Tor and Muntatschinig locations.

Table 3: Local accuracy scores between *in-situ* data and modelled TSEB-ET for the eight Eddy Covariance towers incorporated in this study.

Site name	Landcover	R	RMSE	MB
IT-Lsn	vineyard	0.93	0.73	0.45
IT-MBo		0.71	1.02	-0.16
IT-MtM	grassland	0.39	2.59	-1.47
IT-MtP		0.74	2.12	2.06
IT-Tor		0.38	1.89	-1.51
FR-Pue		-0.18	2.06	0.82
IT-Ren	forest	0.62	2.10	-1.72
IT-SR2		0.23	1.86	1.18

In parallel, the average accuracy scores over forested areas are the least satisfactory when predicting daily gridded ET. The Pearson correlation coefficient is negligible (R = 0.04), and the RMSE error is around 2 mm day^{-1} (Figure 3b). Moreover, as seen in Table 3, regardless of the site and forest type (evergreen broadleaf or needleleaf forest), the TSEB-ET maps have high RMSE scores ranging from 1.86 mm to 2.10 mm per day with big over(under)estimation of 1.18 mm day^{-1} (-1.72 mm day^{-1}) for IT-SR2 and IT-Ren, respectively. The poor accuracy at forested sites might be related to their complex tree structures and multilayer composition which is not considered in Sen-ET. This means that controlling parameters for the model obtained from remote sensing (Copernicus Sentinels) and climate reanalysis data (ERA5) may not capture spatial variability of vegetation elements often accompanied with shadows.

To sum up, the evaluation metrics depict a high landcover dependency with the best accuracy for the vineyard site in IT-Lsn and the grass-covered plateau of IT-MBo yielding an average RMSE ranging from 0.7 mm day^{-1} to 1 mm day^{-1} and a mean R coefficient of 0.7-0.9. Despite 100-m Sentinel-based inputs, it is still challenging to accurately estimate ET over mountains and forest areas, like alpine grasslands (IT-MtM, IT-MtP, and IT-Tor) and Mediterranean forests in FR-Pue and It-SR2. For these ecosystems mean statistics scores are less satisfactory with RMSEs ranging from 1.86 mm day^{-1} at IT-SR2 site to 2.59 mm day^{-1} at IT-MtM (Table 3). This might appear due to several reasons. First, these sites are characterized by patched land covers, including grazed grass, sparsely distributed bushes, and trees, along with their complex multilayer structure exposed to shadows, which contributes to spatial heterogeneities within 100-m ET pixels. Furthermore, high-elevation grasslands are strongly affected by complex interactions between surface energy balance components having an impact on final ET estimates (Mildrexler, 2011). These findings are in line with the outcomes of *Bartkowiak et al.* (2022) where MODIS LST-based TSEB-PT achieved a moderate agreement against local LE records at Muntatschinig sites (R^2 close to 0.61), even though the model was forced with ground-derived meteorological inputs at very high spatiotemporal resolution.

On the other side, the 10-day reflectance composites obtained from Sentinel-2 L2A may not be temporally representative of vegetation conditions corresponding to Sentinel-3 acquisition dates, especially for areas with fast canopy changes due to harvesting, livestock grazing, and mowing events. Consequently, this also affects downscaled LST images that are predicted from the S2 SR mosaics neglecting time-varying characteristics of the land surface.

470   Apart from the lagged S2 response, the data driven DMS sharpener algorithm depends on thermal variability of 1-km S3
pixels, which constrains its predictions within those cell values used for model training (see Sect. 3.2 for more details). This
could contribute to bigger differences between *in-situ* and modelled ET.

      As mentioned before, we use the existing TSEB-PT configuration with the global ERA5 data to scale up the ET retrieval
over the Mediterranean region. The ET models are controlled by climate inputs derived from 31-km fields, which might
475   negatively influence energy fluxes and daily ET. As reported by *Fisher et al.* (2017), these data might not capture local climate
conditions and their rapid changeability over complex areas. By applying 31-km meteorological inputs together with net and
downward shortwave radiation, ERA5 parameters do not reflect spatial variability of the land resulting in a mismatch between
EC tower-derived ET values and their corresponding gridded estimates.

4.2 Daily ET mosaics

480   The last step of the processing workflow includes the generation of daily ET composites from S2 tile-cropped ET grids for
each basin separately. In this regard, we create daily mosaics with respect to acquisition days of the SL_2_LST products
considering two different product dissemination units (PDUs) that include Sentinel-3 images distributed in half-orbit stripes
and 3-min frame mode. Given many ET maps with the same date within an identical Sentinel-2 tile, which can happen to the
frame scenes with smaller spatial extents, ET granules are first combined by applying an average function over overlapping
485   areas for each product derived from individual S3 SLSTR instruments. Next, day-coincident ET grids obtained from Sentinel-
3A and Sentinel-3B satellites are together composted. In the case of single frame acquisitions and large stripe images that
processing step is skipped. Finally, all ET granules are fused concerning the S2 tile-wise basin coverage (see Appendix B)
where overlaying areas of different S2 tiles are also averaged. Low-quality pixels, mostly affected by clouds and lack of the
input parameters for the TSEB, are flagged as NaN values. To make the datasets harmonized and consistent with other
490   hydrological products all mosaics are reprojected to the WGS84 coordinate system using a uniform MR domain grid (Massari
et al., 2022).

      The development of the ET mosaics composting scheme has been performed through the SNAP Graphical Processing Tool
(GPT).

      Figure 4 presents the final ET maps in the summer of 2018 for the MR catchments that include Ebro, Hérault, Medjerda, and
495   Po basins.
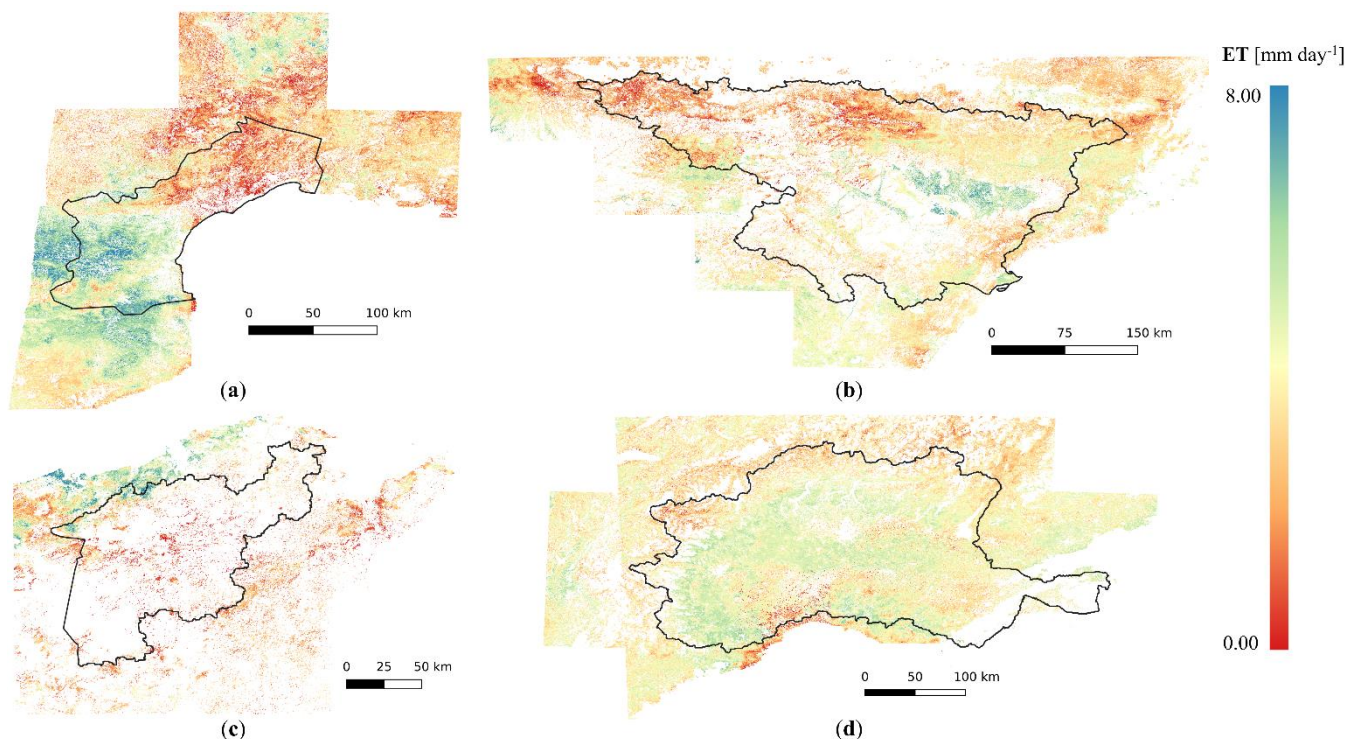
Figure 4: Examples of 100-m ET mosaics from the third week of August 2018 for (a) Languedoc-Roussillon with Hérault (15.08), (b) Ebro (13.08), (c) Medjerda (16.08), and (d) Po (15.08) basins. The entire grids are cropped following the Sentinel-2 tiling scheme. Missing data (in white) are related to Sentinel-3 cloud masks and anthropogenic surfaces. Since we focus on terrestrial ET, water bodies are also removed.

500   From a visual assessment of the daily mosaics, regardless of study areas, no notable irregularities in evaporation are observed (Figure 4). Daily ET composites follow both landscape and season-induced ET patterns across the study areas. As shown in Figure 4, between the 13th and 15th of August, the Ebro and Po basins contain lower ET values over mountain regions of the northern Apennines and the southern Alps between Italy and Switzerland, along with the Pyrenees and Iberian Range in Spain (Figure 4b, d). At the same time, the central parts of the Ebro catchment, despite semi-arid climatic conditions, receive

505   higher ET values, which indicates a strong impact on agricultural activities where many parcels are irrigated during the growing season. Similarly, more intense ET can be observed in the western Alps and across the Po river depression covered with extensive canal systems allocated to farming and food production. In parallel, Hérault exhibited two different ET zones on the 15th of August 2018 (Figure 4a). While the southwest part of the Pyrenees is characterized by greater daily ET rates, the remaining area represented by arable land indicates generally lower evaporation proving possible water stress in the LR region

510   characterized by hot and dry summers. The daily composite of the Medjerda basin from August 16th, despite many invalid pixels in the image, depicts geographically reasonable TSEB model estimates (Figure 4c). Namely, the seaside area in the north represents irrigated fields where ET is expected to be larger compared to the southern zone with limited water resources due to the arid climate.

Nevertheless, the ET product contains areas where TSEB is incapable of estimating ET. Apart from masked surfaces like
515   water bodies and other non-vegetated classes, we can observe an impact of cloud cover (CC) in the final ET product. Even
though we reduce this effect by combining decadal Sentinel-2 composites, which minimize cloud probability, and daily
Sentinel-3 LST that by its high revisit time enables relatively continuous ET monitoring without big temporal gaps between
observations, cloud occurrence is still present in the daily ET mosaics. This is especially visible over the Medjerda catchment
where nearly 86% of the total vegetated surface area contains non-valid pixels (Figure 5a). Seaside areas and the central part
520   of the MB might be affected by overcast conditions, while the southern part is covered by desert and sparse vegetation. In
addition, smaller number of S2 acquisitions outside Europe might have an impact on higher CC percentage in Tunisia. On the
other side, the three remaining basins (i.e., EB, HB, and PB) are generally influenced by relatively similar frequencies of
overcast conditions that range between 62% for Hérault and 69% for Po and Ebro as shown in Figure 5a. Similar to Medjerda
region, they are located in the close range of Mediterranean Sea, and in case of Ebro and Po they include extent mountain
525   ranges, like the Alps and Pyrenees, frequently exposed to cloud contamination.

(a)   **(b)**
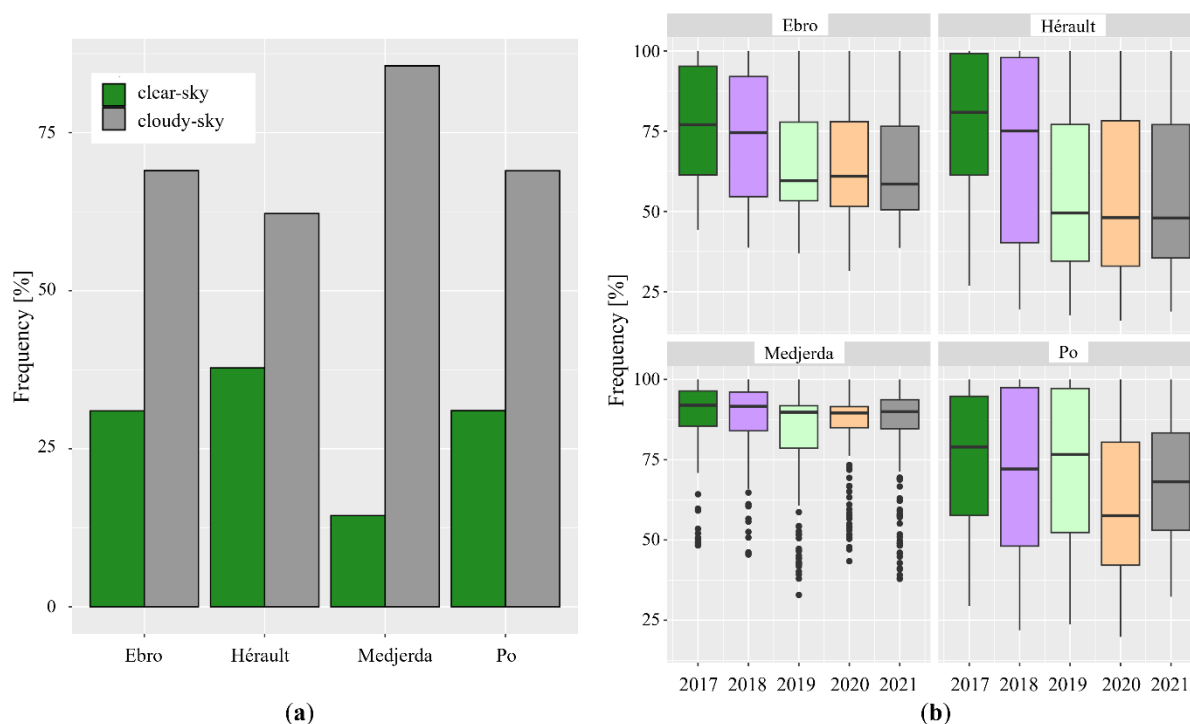
Figure 5: General overview on the sky conditions for the final ET mosaics over each basin (EB, HB, MB, PB) considering: (a) clear and overcast conditions at Sentinel-3 and Sentinel-2 overpass time for the period 2017-2021, (b) the distribution of cloudy-sky conditions for each separate year. Note that non-vegetated surfaces are excluded from this analysis. In order to minimize other disturbing factors such as a seasonal snow cover, our time of interest covers the period during growing season.

530   Nonetheless, if we scrutinize the cloud occurrence over the entire ET collection at annual basis (2017-2021) the frequency of
cloudy events fluctuates from day to day (Figure 5b). For example, considering the geographical proximity of Ebro and Hérault
basins, we can observe higher values of cloud coverage within the period 2017-2018 with an average CC (CC$_{mean}$) equal to

74%, while for 2019-2021 clear sky pixels correspond to 40% of all available grid cells. At the same time, the interquartile ranges (IQRs) are relatively consistent over time for each of two catchments. On average, cloud cover frequency over Po basin differs between years with the biggest IQRs values in 2017-2019 (CC_{mean} = 72%), and smaller cloud effect yielding 64% for 2-year period between 2020 and 2021 (Figure 5b). In contrast, Medjerda region is the most affected by clouds with the highest cloud coverage and lowest CC variability among all basins over the entire time period. As depicted in Figure 5b, an average percentage of invalid pixels over the catchment ranges from 83% in 2019 to 88% in 2017. In general, sky conditions with more than half of clear-sky pixels are observed beyond the IQRs.

5 Code and data availability

The 100-m ET maps are the contribution of EURAC Research to the 4DMED-Hydrology project funded by the European Space Agency (*https://www.4dmed-hydrology.org/*). This dataset is available for the period 2017-2021 for each separate Mediterranean basin that includes Ebro, Hérault, Medjerda, and Po catchments. ET maps are produced for each month (Jan-Dec) of the year in the form of daily observations. The spatial extent corresponds to Sentinel-2 tiling grids overlapping with the study domains (Figure 4). Each layer contains one single band with daily ET values [mm/day] corresponding to Sentinel-3 acquisition day. Invalid pixels, mainly due to vegetation masks, cloud contamination, and lack of input data for the TSEB model, are filled with NaN values. ET outputs are generated in Cloud Optimized GeoTIFF (COG) format with metadata included in the file attributes. A COG is a regular GeoTIFF file, optimized for use in a cloud environment, ready to be hosted on a HTTP(S) file server, with an internal organization that enables more efficient workflows on the cloud. It facilitates data download through HTTP(S) data request and allows a user to crop data according to area of interests. The importance of metadata availability in the COG file is twofold: on one side it offers the chance to evaluate the data without opening it; on the other side, this information has been used to fill a catalogue following the SpatioTemporal Asset Catalog (STAC) specifications that provides a common structure for describing and cataloguing spatiotemporal assets (*https://stacspec.org/en/*). To query the ET data in the STAC catalogue, a relevant STAC documentation is available together with a Python snippet code for massive data download via the Environmental Data Platform (*https://edp-portal.eurac.edu/discovery/*). Alternatively, we provide an additional data link to manually download the entire basin-based ET collection.

As mentioned before, daily ET datasets are accessible through the Environmental Data Platform of EURAC Research under the Creative Commons Attribution 4.0 License (CC BY 4.0). Note that if you use these datasets, you are kindly asked to include the following references concerning the four study domains:

(1) For Ebro: https://doi.org/10.48784/b90a02d6-5d13-4acd-b11c-99a0d381ca9a (Bartkowiak et al., 2023a),

(2) For Hérault: https://doi.org/10.48784/fb631817-189f-4b57-af6a-38cef217bad3 (Bartkowiak et al., 2023b),

(3) For Medjerda: https://doi.org/10.48784/70cd192c-0d46-4811-ad1d-51a09734a2e9 (Bartkowiak et al., 2023c),

(4) For Po: https://doi.org/10.48784/7abdbd94-ddfe-48df-ab09-341ad2f52e47 (Bartkowiak et al., 2023d).

All code routines developed for the entire processing workflow are available upon request from the authors.

6 Conclusions

Although ET plays a key role in the hydrological cycle and represents a nexus between energy, water, and carbon exchange, its availability is constrained either to short-range *in-situ* measurements or freely available satellite-derived ET data at coarse spatial resolutions ($\geq$ 0.5 km). Thus, the generation of HR ET datasets is of high importance among scientists, but also of governmental institutions and agricultural communities to advance hydrological cycle monitoring and sustainable water management.

Motivated by the lack of ET data at a high spatiotemporal resolution over the Mediterranean region (MR), we build an automatic workflow to provide 5-year time-series of 100-m daily ET product (2017-2021) as a helpful tool in the context of recurring drought events across the MR. Specifically, we utilize a globally applicable TSEB-PT approach with a reduced number of inputs that minimize its complexity, being an advantage for high-volume processing at large scales. The model is physically based and has a long history of successful research studies that confirm its maturity and stability. Results demonstrate that the developed TSEB-ET workflow is capable of predicting ET in a robust manner.

The daily composites generally follow the seasonal patterns of the canopy over the study areas (see Sect. 2.1) with higher ET values over irrigated areas and lower estimates over rainfed vegetation like natural grasslands and forests. The generated time-series have reasonable scores compared to time-coincident local records from Eddy Covariance stations. Nevertheless, the prediction skill of the Copernicus-driven TSEB-ET exhibits landcover dependency with the best accuracy results for agricultural areas and less satisfactory outcomes in forests. The validation scores confirm a strong agreement between gridded data and *in-situ* measurements, especially over relatively uniform and flat areas represented by vineyard and grassland yielding an average R and mean error equal to 0.80 and 0.85 mm day^{-1}, respectively. In contrast, on a level of single landcover classes, RMSEs (Rs) range from 1.86 (-0.18) in forested areas to 2.59 (0.74) for grasslands considering all remaining sites in this study.

Even though the Priestley-Taylor TSEB gives very promising outcomes for plain and homogenous areas, which makes it a perfect candidate for lowland agriculture activities, site locations across biomes, like steep mountain grasslands and forested sites, create some confusion to the model mainly due to inability of gridded inputs to represent complex canopy structure and its heterogeneity together with highly changing meteorological conditions (Elfarkh et al., 2020). Notably, TSEB-ET estimates are affected by spatial heterogeneities of the study areas, and consequently pixel size of gridded input parameters. Given the temporal and spatial frames of this project, the validation is conducted against EC towers, 62.5% of which are located in the Alps. Thus, future work should be extended to more validation sites with relatively simple terrain and homogenous vegetation to minimize environmental impacts on the TSEB-PT performance. In parallel, additional work shall be focused on the implementation of better-quality inputs such as climate forcings from 3-km solar radiation acquired by MSG SEVIRI and 5.5 km CERRA reanalysis datasets. Moreover, considering ET dependency on LST accuracy, the DMS sharpener together with Sentinel-2 and -3 cloud masks shall be enriched. Even though a more rigorous cloud layer for the TIR sensor is under active debate among scientists (*https://thermal2023.esa.int/*), the most recent S3 SLSTR Validation Report comes from 2017 providing unimproved data. Considering irregular ET observations affected by cloudy-sky conditions, future research should

also concentrate on a data-driven approach to recover overcast cell grids. Furthermore, to capture time-induced characteristics of the land surface, LST downscaling, and TSEB-PT models might be additionally driven by more frequent variables rather than 10-day Sentinel-2 reflectances. The temporal mismatch between S2 and S3 can be solved by applying Harmonized Landsat-Sentinel imagery, which in parallel minimizes the probability of cloudiness. Consequently, due to some inaccuracies in the Sen2Cor cloud mask, other products like Sen2cloudless and Fmask shall be integrated into the workflow. The enhanced products would be a valuable tool to accurately estimate the components of the terrestrial water cycle on a regional scale and over heterogeneous ecosystems.

Appendices

Appendix A1

630 **Fig. A1: Locations of the Eddy Covariance towers used for validating the ET product at (a) IT-MtM (source:** *https://browser.lter.eurac.edu/*), **(b) IT-MtP (source:** *https://browser.lter.eurac.edu/*), **(c) IT-Lsn (source:** *https://www.icos-italy.it/lison-it-lsn/*), **(d) IT-Tor (source:** *https://www.icos-italy.it/elementor-2052/*), **(e) IT-Ren (source:** *https://deims.org/5d32cbf8-ab7c-4acb-b29f-600fec830a1d*), **(f) FR-Pue (source:** *https://meta.icos-cp.eu/resources/stations/ES_FR-Pue*), **(g) IT-SR2 (source:** *https://meta.icos-cp.eu/resources/stations/ES_IT-SR2*), **(h) IT-MBo (source:** *Sakowska et al., 2014*) **sites.**
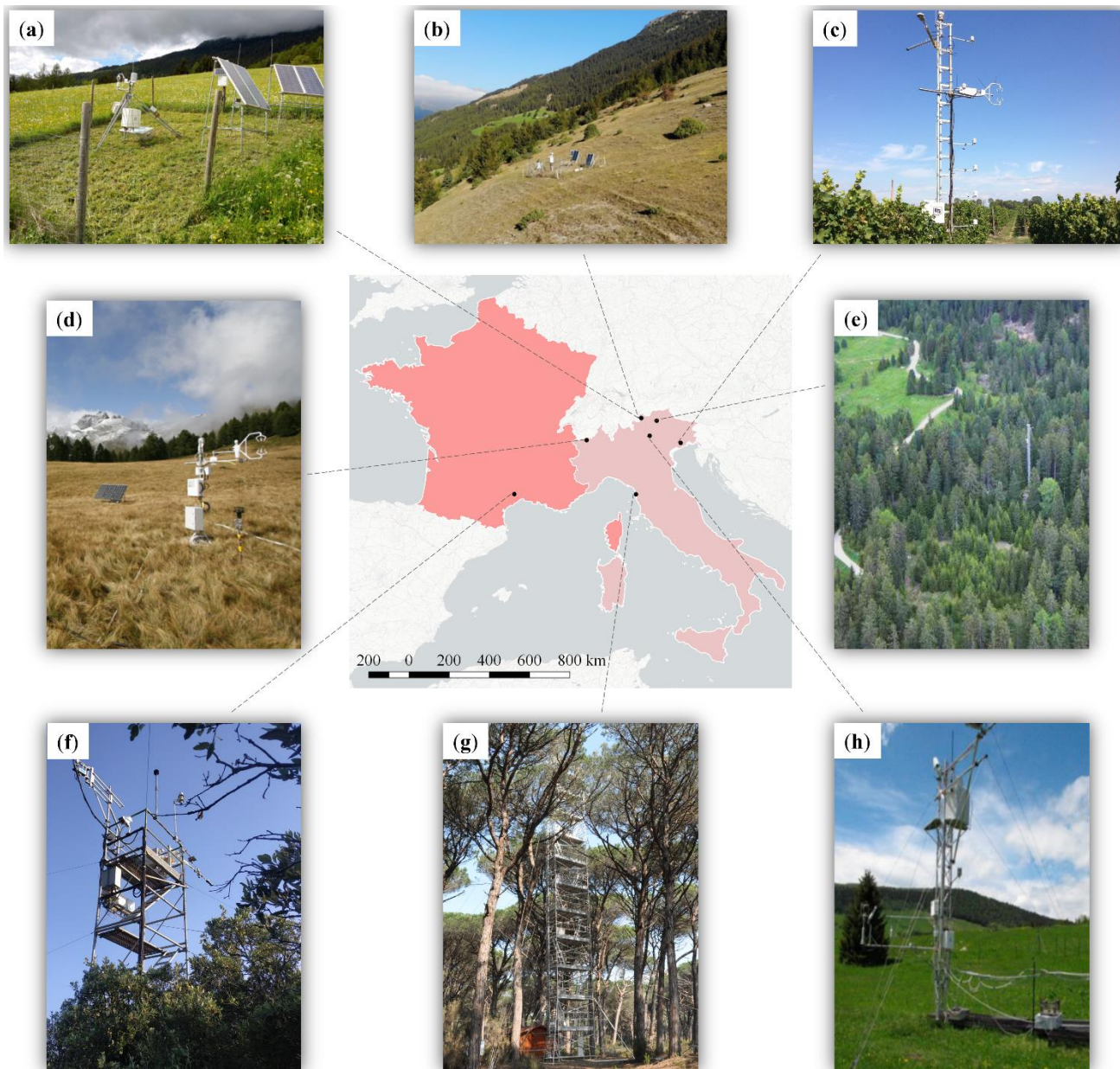
635 **Appendix B**

Fig. B1: Spatial coverage of Sentinel-2 tiles together with their overlapping areas for (a) Po, (b) Ebro, (c) Medjerda, (d) Hérault basins. Each tile (in green) contains respective identification number corresponding to Sentinel-2 tiling system as explained at *https://sentinels.copernicus.eu/web/sentinel/missions/sentinel-2/data-products*.
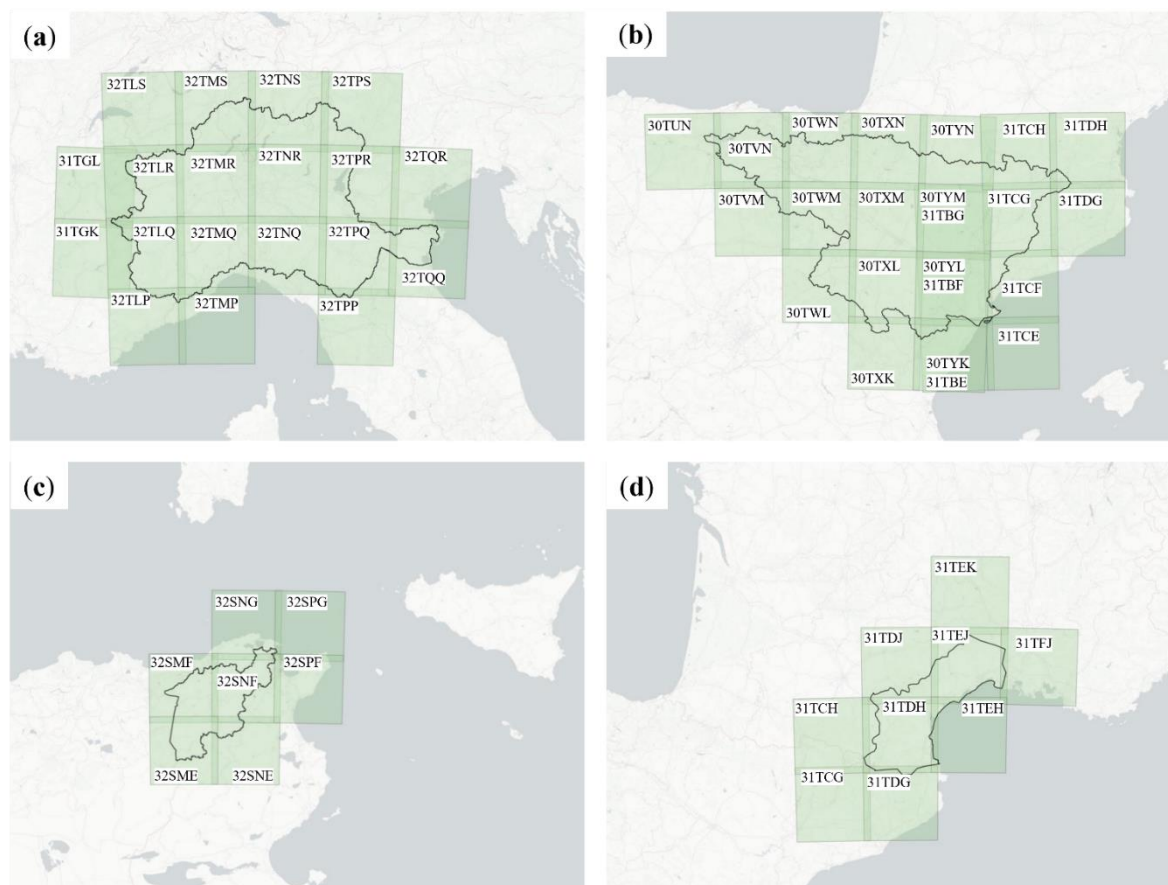
640 **Author contribution**

MC and PB contributed to the research conceptualization and its implementation. Data collection, processing, and data analysis were conducted by PB with the assistance of BV. AJ and BV were responsible for the cloud computing infrastructure setup and the database management. MC supervised and supported the entire work. The original draft was prepared by PB, and then revised in collaboration with MC, BV, and AJ.

645 **Competing interests**

The authors of this paper declare no conflict of interest.

Acknowledgements

This work was supported by European Space Agency in the framework of 4DMED-Hydrology project: "Developing an advanced, high-resolution, and consistent reconstruction of the Mediterranean terrestrial water cycle" (ESA Contract No. 4000136272/21/I-EF). The authors would like to thank Petra Hulsman and Diego Miralles for preparing and sharing pre-processed in-situ data from Eddy Covariance towers.

650

Abbreviations and acronyms

The following abbreviations and acronyms are used in this work:

α_{PT}	Priestley-Taylor coefficient for potential transpiration (default = 1.26)
CC	Cloud cover
CERRA	Copernicus European Regional ReAnalysis
DMS	Data Mining Sharpener
DT	Decision Trees
ECMWF	European Centre for Medium-Range Weather Forecasts
ECOSTRESS	ECOsystem Spaceborne Thermal Radiometer Experiment
EFDC	European Fluxes Database Cluster
EO	Earth Observation
EODC	Earth Observation Data Centre
ERA5	European ReAnalysis V5
ESA	European Space Agency
ET	Evapotranspiration
FAO	Food and Agriculture Organization
GLDAS	Global Land Data Assimilation System
GLEAM	Global Land Evaporation Amsterdam Model
GPT	Graphical Processing Tool
HR	High resolution
ICOS	Integrated Carbon Observation System
IQR	Interquartile range
LAI	Leaf Area Index
LC	Landcover
LIDAR	LIght Detection And Ranging
LSA-SAF	Land Surface Analysis - Satellite Application Facility
LST	Land Surface Temperature
LSTM	Copernicus Land Surface Temperature Monitoring
MODIS	Moderate Resolution Imaging Spectroradiometer
MR	Mediterranean Region
MSG	Meteosat Second Generation
MSI	MultiSpectral Instrument
NASA	National Aeronautics and Space Administration
PDU	Product Dissemination Unit
Sen-ET	Sentinels for Evapotranspiration
SEVIRI	Spinning Enhanced Visible and InfraRed Imager

SGB	Surface Biology and Geology
SLSTR	Sea and Land Surface Temperature Radiometer
S-NPP	Suomi National Polar-orbiting Partnership
SR	Surface Reflectance
SRTM	Shuttle Radar Topography Mission
STAC	Spatio Temporal Asset Catalogue
TIR	Thermal Infrared
TRISHNA	Thermal infraRed Imaging Satellite for High-resolution Natural resource Assessment
(T)SEB	(Two-)Source Energy Balance
VIIRS	Visible Infrared Imaging Radiometer Suite
VSWIR	Visible ShortWave InfraRed
WaPOR	Water Productivity through Open access of Remotely sensed derived data
WGS84	World Geodetic System 1984

References

655 Alfieri, L., Avanzi, F., Delogu, F., Gabellani, S., Bruno, G., Campo, L., Libertino, A., Massari, C., Tarpanelli, A., Rains, D. and Miralles, D. G.: High-resolution satellite products improve hydrological modeling in northern Italy. Hydrology and Earth System Sciences, 26(14), pp.3921-3939, 2022.

Allen, R. G., Howell, T. A., Pruitt, W. O., Walter, I. A. and Jensen, M. E.: Lysimeters for evapotranspiration and environmental measurements. ASCE, 1991.

660 Allen, R. G., Pereira, L. S., Raes, D., and Smith M.: Crop Evapotranspiration: Guidelines for Computing Crop Water Requirements (FAO Irrigation and Drainage Paper), 328 pp., FAO—Food and Agric. Organ. of the U. N., Rome, 1998.

Anderson, M. C., Allen, R. G., Morse, A. and Kustas, W. P.: Use of Landsat thermal imagery in monitoring evapotranspiration and managing water resources. Remote Sensing of Environment, 122, pp.50-65, 2012.

Anderson, M. C., Yang, Y., Xue, J., Knipper, K. R., Yang, Y., Gao, F., Hain, C. R., Kustas, W. P., Cawse-Nicholson, K., Hulley, G. and
665 Fisher, J. B.: Interoperability of ECOSTRESS and Landsat for mapping evapotranspiration time series at sub-field scales. Remote Sensing of Environment, 252, p.112189, 2021.

Babaeian, E., Paheding, S., Siddique, N., Devabhaktuni, V. K. and Tuller, M.: Short-and mid-term forecasts of actual evapotranspiration with deep learning. Journal of Hydrology, 612, p.128078, 2022.

Bai, P. and Liu, X.: Intercomparison and evaluation of three global high-resolution evapotranspiration products across China. Journal of
670 hydrology, 566, pp.743-755, 2018.

Barella-Ortiz, A., Quintana-Seguí, P., Clavera-Gispert, R., Munier, S., Merlin, O., Olivera-Guerra, L. E., Altés, V., Villar, J. M., Brocca, L., Dari, J. and Modanesi, S.: Analysis of the impact of different irrigation scenarios on the water balance of the Ebro River Basin by means of a LSM and remote sensing irrigation estimations (No. EGU23-14091). Copernicus Meetings, 2023.

Bartkowiak, P., Ventura, B., Jacob, A., and Castelli, M.: Daily evaporation product – Ebro basin (Version v1) [Data set]. Institute for Earth
675 Observation. https://doi.org/10.48784/B90A02D6-5D13-4ACD-B11C-99A0D381CA9A, 2023a.

Bartkowiak, P., Ventura, B., Jacob, A., and Castelli, M.: Daily evaporation product – Hérault basin (Version v1) [Data set]. Institute for Earth Observation. https://doi.org/10.48784/FB631817-189F-4B57-AF6A-38CEF217BAD3, 2023b.

Bartkowiak, P., Ventura, B., Jacob, A., and Castelli, M.: Daily evaporation product – Medjerda basin (Version v1) [Data set]. Institute for Earth Observation. https://doi.org/10.48784/70CD192C-0D46-4811-AD1D-51A09734A2E9, 2023c.

680   Bartkowiak, P., Ventura, B., Jacob, A., and Castelli, M.: Daily evaporation product – Po basin (Version v1) [Data set]. Institute for Earth Observation. https://doi.org/10.48784/7ABDBD94-DDFE-48DF-AB09-341AD2F52E47, 2023d.

Bartkowiak, P., Castelli, M., Colombo, R. and Notarnicola, C.: Two-source energy balance modeling of evapotranspiration with thermal remote sensing at different spatial resolutions: a case study of the European Alps. In Remote Sensing for Agriculture, Ecosystems, and Hydrology XXIV (Vol. 12262). SPIE, 2022, October.

685   Bastiaanssen, W. G. M., Cheema, M. J. M., Immerzeel, W. W., Miltenburg, I. J. and Pelgrum, H.: Surface energy balance and actual evapotranspiration of the transboundary Indus Basin estimated from satellite measurements and the ETLook model. Water Resources Research, 48(11), 2012.

Bellvert, J., Jofre-Ĉekalović, C., Pelechá, A., Mata, M. and Nieto, H.: Feasibility of using the two-source energy balance model (TSEB) with Sentinel-2 and Sentinel-3 images to analyze the spatio-temporal variability of vine water status in a vineyard. Remote Sensing, 12(14),
690   p.2299, 2020.

Bhattarai, N. and Wagle, P.: Recent advances in remote sensing of evapotranspiration. Remote Sensing, 13(21), p.4260, 2021.

Blatchford, M. L., Mannaerts, C. M., Njuki, S. M., Nouri, H., Zeng, Y., Pelgrum, H., Wonink, S. and Karimi, P.: Evaluation of WaPOR V2 evapotranspiration products across Africa. Hydrological processes, 34(15), pp.3200-3221, 2020.

Boulmaiz, T., Boutaghane, H., Abida, H., Saber, M., Kantoush, S. A. and Tramblay, Y.: Exploring the spatio-temporal variability of
695   precipitation over the Medjerda Transboundary Basin in North Africa. Water, 14(3), p.423, 2022.

Buttar, N. A., Yongguang, H., Shabbir, A., Lakhiar, I. A., Ullah, I., Ali, A., Aleem, M. and Yasin, M. A.: Estimation of evapotranspiration using Bowen ratio method. IFAC-PapersOnLine, 51(17), pp.807-810, 2018.

Cambrea, L., Lafon, C. and Mayoux, L.: Live from the regions–Vine irrigation in the former Languedoc-Roussillon region: production potential maintained through water savings. Sciences Eaux & Territoires, (34 bis), pp.28-33, 2020.

700   Cammalleri, C., Anderson, M. C., Gao, F., Hain, C. R. and Kustas, W. P.: Mapping daily evapotranspiration at field scales over rainfed and irrigated agricultural areas using remote sensing data fusion. Agricultural and forest meteorology, 186, pp.1-11, 2014.

Castelli, M.: Evapotranspiration Changes over the European Alps: Consistency of Trends and Their Drivers between the MOD16 and SSEBop Algorithms. Remote Sensing, 13(21), p.4316, 2021.

Cawse-Nicholson, K. and Anderson, M.: ECOSTRESS Level-3 DisALEXI-JPL Evapotranspiration (ECO3ETALEXI) Algorithm
705   Theoretical Basis Document. Jet Propulsion Laboratory California Institute of Technology: Pasadena, CA, USA, 2021.

Chattopadhyay, N. and Hulme, M.: Evaporation and potential evapotranspiration in India under conditions of recent and future climate change. Agricultural and Forest Meteorology, 87(1), pp.55-73, 1997.

Chintala, S., Harmya, T. S., Kambhammettu, B. V. N. P., Moharana, S. and Duvvuri, S.: Modelling high-resolution Evapotranspiration in fragmented croplands from the constellation of Sentinels. Remote Sensing Applications: Society and Environment, 26, p.100704, 2022.

710   Coenders-Gerrits, M., Schilperoort, B. and Jiménez-Rodríguez, C.: Evaporative processes on vegetation: an inside look. Precipitation partitioning by vegetation: A global synthesis, pp.35-48, 2020.

Cui, Y., Song, L. and Fan, W.: Generation of spatio-temporally continuous evapotranspiration and its components by coupling a two-source energy balance model and a deep neural network over the Heihe River Basin. Journal of Hydrology, 597, p.126176, 2021.

Dari, J., Brocca, L., Modanesi, S., Massari, C., Tarpanelli, A., Barbetta, S., Quast, R., Vreugdenhil, M., Freeman, V., Barella-Ortiz, A. and
715   Quintana-Seguí, P.: Regional data sets of high-resolution (1 and 6 km) irrigation estimates from space. Earth System Science Data, 15(4), pp.1555-1575, 2023.

Dari, J., Quintana-Seguí, P., Morbidelli, R., Saltalippi, C., Flammini, A., Giugliarelli, E., Escorihuela, M. J., Stefan, V. and Brocca, L.: Irrigation estimates from space: Implementation of different approaches to model the evapotranspiration contribution within a soil-moisture-based inversion algorithm. Agricultural Water Management, 265, p.107537, 2022.

720   Dezsi, Ş., Mîndrescu, M., Petrea, D., Rai, P. K., Hamann, A. and Nistor, M. M.: High-resolution projections of evapotranspiration and water availability for Europe under climate change. International Journal of Climatology, 38(10), pp.3832-3841, 2018.

DHI-GRAS: User Manual For SEN-ET SNAP Plugin. 0–35. Available online: https://www.esa-sen4et.org/static/media/sen-et-user-manual-v1.1.0.2cd617fb322658397542.pdf, 2020.

Douna, V., Barraza, V., Grings, F., Huete, A., Restrepo-Coupe, N. and Beringer, J.: Towards a remote sensing data based evapotranspiration

725   estimation in Northern Australia using a simple random forest approach. Journal of Arid Environments, 191, p.104513, 2021.

Elfarkh, J., Ezzahar, J., Er-Raki, S., Simonneaux, V., Ait Hssaine, B., Rachidi, S., Brut, A., Rivalland, V., Khabba, S., Chehbouni, A. and Jarlan, L.: Multi-scale evaluation of the TSEB model over a complex agricultural landscape in Morocco. Remote Sensing, 12(7), p.1181, 2020.

Fabre, J., Ruelland, D., Dezetter, A. and Grouillet, B.: Simulating past changes in the balance between water demand and availability and

730   assessing their main drivers at the river basin scale. Hydrology and Earth System Sciences, 19(3), pp.1263-1285, 2015.

FAO: AQUASTAT Tunisia fact sheet. https://tableau.apps.fao.org/views/, 2020. Accessed on 07 July 2023.

Ferreira, L. B., da Cunha, F. F., de Oliveira, R. A. and Fernandes Filho, E. I.: Estimation of reference evapotranspiration in Brazil with limited meteorological data using ANN and SVM–A new approach. Journal of Hydrology, 572, pp.556-570, 2019.

Filippucci, P., Brocca, L., Quast, R., Ciabatta, L., Saltalippi, C., Wagner, W. and Tarpanelli, A.: High-resolution (1 km) satellite rainfall

735   estimation from SM2RAIN applied to Sentinel-1: Po River basin as a case study. Hydrology and Earth System Sciences, 26(9), pp.2481-2497, 2022.

Fisher, J. B.: Level-3 Evapotranspiration L3 (ET_PT-JPL) Algorithm Theoretical Basis Document. Technical Report. NASA Jet Propulsion Laboratory, 2018.

Fisher, J. B., Melton, F., Middleton, E., Hain, C., Anderson, M., Allen, R., McCabe, M. F., Hook, S., Baldocchi, D., Townsend, P. A. and

740   Kilic, A.: The future of evapotranspiration: Global requirements for ecosystem functioning, carbon and climate feedbacks, agricultural management, and water resources. Water resources research, 53(4), pp.2618-2626, 2017.

Gao, F., Kustas, W. P. and Anderson, M. C.: A data mining approach for sharpening thermal satellite imagery over land. Remote Sensing, 4(11), pp.3287-3319, 2012.

Gao, X., Zhao, Q., Zhao, X., Wu, P., Pan, W., Gao, X. and Sun, M.: Temporal and spatial evolution of the standardized precipitation

745   evapotranspiration index (SPEI) in the Loess Plateau under climate change from 2001 to 2050. Science of the Total Environment, 595, pp.191-200, 2017.

Gaona, J., Quintana-Seguí, P., Escorihuela, M. J., Boone, A. and Llasat, M. C.: Interactions between precipitation, evapotranspiration and soil-moisture-based indices to characterize drought with high-resolution remote sensing and land-surface model data. Natural Hazards and Earth System Sciences, 22(10), pp.3461-3485, 2022.

750   García-Santos, V., Sánchez, J. M. and Cuxart, J.: Evapotranspiration Acquired with Remote Sensing Thermal-Based Algorithms: A State-of-the-Art Review. Remote Sensing, 14(14), p.3440, 2022.

Gouveia, C. M., Trigo, R. M., Beguería, S. and Vicente-Serrano, S. M.: Drought impacts on vegetation activity in the Mediterranean region: An assessment using remote sensing data and multi-scale drought indicators. Global and Planetary Change, 151, pp.15-27, 2017.

Granata, F., Gargano, R. and de Marinis, G.: Artificial intelligence based approaches to evaluate actual evapotranspiration in wetlands. Science of The Total Environment, 703, p.135653, 2020.

Guzinski, R. and Nieto, H.: Evaluating the feasibility of using Sentinel-2 and Sentinel-3 satellites for high-resolution evapotranspiration estimations. Remote sensing of Environment, 221, pp.157-172, 2019.

Guzinski, R., Nieto, H., Jensen, R., and Mendiguren, G.: Remotely sensed land-surface energy fluxes at sub-field scale in heterogeneous agricultural landscape and coniferous plantation, Biogeosciences, 11, 5021–5046, https://doi.org/10.5194/bg-11-5021-2014, 2014.

Guzinski, R., Nieto, H., Sandholt, I. and Karamitilios, G.: Modelling high-resolution actual evapotranspiration through Sentinel-2 and Sentinel-3 data fusion. Remote Sensing, 12(9), p.1433, 2020.

Heiskanen, J., Brümmer, C., Buchmann, N., Calfapietra, C., Chen, H., Gielen, B., Gkritzalis, T., Hammer, S., Hartman, S., Herbst, M. and Janssens, I. A.: The integrated carbon observation system in Europe. Bulletin of the American Meteorological Society, 103(3), pp.E855-E872, 2022.

Hersbach, H., Bell, B., Berrisford, P., Hirahara, S., Horányi, A., Muñoz-Sabater, J., Nicolas, J., Peubey, C., Radu, R., Schepers, D. and Simmons, A.: The ERA5 global reanalysis. Quarterly Journal of the Royal Meteorological Society, 146(730), pp.1999-2049, 2020.

Hoffmann, H., Nieto, H., Jensen, R., Guzinski, R., Zarco-Tejada, P. and Friborg, T.: Estimating evaporation with thermal UAV data and two-source energy balance models. Hydrology and Earth System Sciences, 20(2), pp.697-713, 2016.

Hu, T., Mallick, K., Hitzelberger, P., Didry, Y., Boulet, G., Szantoi, Z., Koetz, B., Alonso, I., Pascolini-Campbell, M., Halverson, G. and Cawse-Nicholson, K.: Evaluating European ECOSTRESS Hub Evapotranspiration Products Retrieved from Three Structurally Contrasting SEB Models over Europe, 2022.

Hu, X., Shi, L., Lin, G. and Lin, L.: Comparison of physical-based, data-driven and hybrid modeling approaches for evapotranspiration estimation. Journal of Hydrology, 601, p.126592, 2021.

Jain, S. K., Nayak, P. C. and Sudheer, K. P.: Models for estimating evapotranspiration using artificial neural networks, and their physical interpretation. Hydrological Processes: An International Journal, 22(13), pp.2225-2234, 2008.

Jiang, S., Wei, L., Ren, L., Xu, C. Y., Zhong, F., Wang, M., Zhang, L., Yuan, F. and Liu, Y.: Utility of integrated IMERG precipitation and GLEAM potential evapotranspiration products for drought monitoring over mainland China. Atmospheric Research, 247, p.105141, 2021.

Kljun, N., Calanca, P., Rotach, M. W. and Schmid, H. P.: A simple two-dimensional parameterisation for Flux Footprint Prediction (FFP). Geoscientific Model Development, 8(11), pp.3695-3713, 2015.

Konapala, G., Mishra, A. K., Wada, Y. and Mann, M. E.: Climate change will affect global water availability through compounding changes in seasonal precipitation and evaporation. Nature communications, 11(1), p.3044, 2020.

Li, B., H. Beaudoing, and M. Rodell, NASA/GSFC/HSL: GLDAS Catchment Land Surface Model L4 daily 0.25 x 0.25 degree V2.0, Greenbelt, Maryland, USA, Goddard Earth Sciences Data and Information Services Center (GES DISC), Accessed: [20.06.2023], 10.5067/LYHA9088MFWQ, 2018.

Li, W., Ni, L., Li, Z. L., Duan, S. B. and Wu, H.: Evaluation of machine learning algorithms in spatial downscaling of MODIS land surface temperature. IEEE Journal of Selected Topics in Applied Earth Observations and Remote Sensing, 12(7), pp.2299-2307, 2019.

Liu, K., Su, H., Li, X. and Chen, S.: Development of a 250-m downscaled land surface temperature data set and its application to improving remotely sensed evapotranspiration over large landscapes in northern China. IEEE Transactions on Geoscience and Remote Sensing, 60, pp.1-12, 2020.

López López, P., Sutanudjaja, E. H., Schellekens, J., Sterk, G. and Bierkens, M. F.: Calibration of a large-scale hydrological model using satellite-based soil moisture and evapotranspiration products. Hydrology and Earth System Sciences, 21(6), pp.3125-3144, 2017.

Lorenzo-González, M. A., Quílez, D. and Isidoro, D.: Factors controlling the changes in surface water temperature in the Ebro River Basin. Journal of Hydrology: Regional Studies, 47, p.101379, 2023.

Maes, W. H. and Steppe, K.: Estimating evapotranspiration and drought stress with ground-based thermal remote sensing in agriculture: a
795 review. Journal of experimental botany, 63(13), pp.4671-4712, 2012.

Main-Knorn, M., Pflug, B., Louis, J., Debaecker, V., Müller-Wilm, U. and Gascon, F.: Sen2Cor for sentinel-2. In Image and Signal Processing for Remote Sensing XXIII (Vol. 10427, pp. 37-48). SPIE, 2017, October.

Mallick, K., Jarvis, A. J., Boegh, E., Fisher, J. B., Drewry, D. T., Tu, K. P., Hook, S. J., Hulley, G., Ardö, J., Beringer, J. and Arain, A.: A Surface Temperature Initiated Closure (STIC) for surface energy balance fluxes. Remote Sensing of Environment, 141, pp.243-261, 2014.

800 Maselli, F., Papale, D., Chiesi, M., Matteucci, G., Angeli, L., Raschi, A. and Seufert, G.: Operational monitoring of daily evapotranspiration by the combination of MODIS NDVI and ground meteorological data: Application and evaluation in Central Italy. Remote Sensing of Environment, 152, pp.279-290, 2014.

Mao, Q., Peng, J. and Wang, Y.: Resolution enhancement of remotely sensed land surface temperature: Current status and perspectives. Remote Sensing, 13(7), p.1306, 2021.

805 Martens, B., Miralles, D. G., Lievens, H., Van Der Schalie, R., De Jeu, R. A., Fernández-Prieto, D., Beck, H. E., Dorigo, W. A. and Verhoest, N. E.: GLEAM v3: Satellite-based land evaporation and root-zone soil moisture. Geoscientific Model Development, 10(5), pp.1903-1925, 2017.

Massari, C., Modanesi, S., Dari, J., Gruber, A., De Lannoy, G. J., Girotto, M., Quintana-Seguí, P., Le Page, M., Jarlan, L., Zribi, M. and Ouaadi, N.: A review of irrigation information retrievals from space and their utility for users. Remote Sensing, 13(20), p.4112, 2021.

810 Massari, C., Tarpanelli, A., Aires, F., Alfieri, L., Avanzi, F., Barbetta, S., Bechtold, M., Brocca, L., Camici, S., Castelli, M. and Ciabatta, L.: 4DMED-Hydrology: capitalizing high resolution Earth Observation data for a consistent reconstruction of the Mediterranean terrestrial water cycle, 2022.

McShane, R. R., Driscoll, K. P. and Sando, R.: A review of surface energy balance models for estimating actual evapotranspiration with remote sensing at high spatiotemporal resolution over large extents. Scientific Investigations Report, (2017-5087), 2017.

815 Mildrexler, D. J., Zhao, M. and Running, S. W.: A global comparison between station air temperatures and MODIS land surface temperatures reveals the cooling role of forests. Journal of Geophysical Research: Biogeosciences, 116(G3), 2011

Miralles, D. G., Holmes, T. R. H., De Jeu, R. A. M., Gash, J. H., Meesters, A. G. C. A. and Dolman, A. J.: Global land-surface evaporation estimated from satellite-based observations. Hydrology and Earth System Sciences, 15(2), pp.453-469, 2011.

Monteith, J. L.: Evaporation and environment. In Symposia of the society for experimental biology (Vol. 19, pp. 205-234). Cambridge
820 University Press (CUP) Cambridge, 1965.

Mu, Q., Heinsch, F. A., Zhao, M. and Running, S.W.: Development of a global evapotranspiration algorithm based on MODIS and global meteorology data. Remote sensing of Environment, 111(4), pp.519-536, 2007.

Musolino, D., De Carli, A. and Massarutto, A.: Evaluation of socio-economic impact of drought events: The case of Po river basin. European Countryside, 9(1), pp.163-176, 2017.

825 Nieto, H., Kustas, W. P., Torres-Rúa, A., Alfieri, J. G., Gao, F., Anderson, M. C., White, W. A., Song, L., Alsina, M. D. M., Prueger, J. H. and McKee, M.: Evaluation of TSEB turbulent fluxes using different methods for the retrieval of soil and canopy component temperatures from UAV thermal and multispectral imagery. Irrigation Science, 37, pp.389-406, 2019.

Norman, J. M., Kustas, W. P. and Humes, K. S.: Source approach for estimating soil and vegetation energy fluxes in observations of directional radiometric surface temperature. Agricultural and Forest Meteorology, 77(3-4), pp.263-293, 1995.

830   Otkin, J. A., Anderson, M. C., Hain, C., Svoboda, M., Johnson, D., Mueller, R., Tadesse, T., Wardlow, B. and Brown, J.: Assessing the evolution of soil moisture and vegetation conditions during the 2012 United States flash drought. Agricultural and forest meteorology, 218, pp.230-242, 2016.

Pastorello, G., Trotta, C., Canfora, E., Chu, H., Christianson, D., Cheah, Y. W., Poindexter, C., Chen, J., Elbashandy, A., Humphrey, M. and Isaac, P.: The FLUXNET2015 dataset and the ONEFlux processing pipeline for eddy covariance data. Scientific data, 7(1), pp.1-27, 2020.

835   Penman, H. L.: Natural evaporation from open water, bare soil and grass. Proceedings of the Royal Society of London. Series A. Mathematical and Physical Sciences, 193(1032), pp.120-145, 1948.

Priestley, C. H. B. and Taylor, R. J.: On the assessment of surface heat flux and evaporation using large-scale parameters. Monthly weather review, 100(2), pp.81-92, 1972.

Pu, R. and Bonafoni, S.: Thermal infrared remote sensing data downscaling investigations: An overview on current status and perspectives.
840   Remote Sensing Applications: Society and Environment, p.100921, 2023.

Rajosoa, A. S., Abdelbaki, C. and Mourad, K. A.: Assessing the impact of climate change on the Medjerda River Basin. Arabian Journal of Geosciences, 15(11), p.1052, 2022.

Reichstein, M., Camps-Valls, G., Stevens, B., Jung, M., Denzler, J. and Carvalhais, N.: Deep learning and process understanding for data-driven Earth system science. Nature, 566(7743), pp.195-204, 2019.

845   Sakowska, K., Gianelle, D., Zaldei, A., MacArthur, A., Carotenuto, F., Miglietta, F., Zampedri, R., Cavagna, M. and Vescovo, L.: WhiteRef: A new tower-based hyperspectral system for continuous reflectance measurements. Sensors, 15(1), pp.1088-1105, 2015.

Senay, G. B., Bohms, S., Singh, R. K., Gowda, P. H., Velpuri, N. M., Alemu, H. and Verdin, J. P.: Operational evapotranspiration mapping using remote sensing and weather datasets: A new parameterization for the SSEB approach. JAWRA Journal of the American Water Resources Association, 49(3), pp.577-591, 2013.

850   Su, Z.: The Surface Energy Balance System (SEBS) for estimation of turbulent heat fluxes. Hydrology and earth system sciences, 6(1), pp.85-100, 2002.

Velpuri, N. M., Senay, G. B., Singh, R. K., Bohms, S. and Verdin, J. P.: A comprehensive evaluation of two MODIS evapotranspiration products over the conterminous United States: Using point and gridded FLUXNET and water balance ET. Remote Sensing of Environment, 139, pp.35-49, 2013.

855   Weerasinghe, I., Bastiaanssen, W., Mul, M., Jia, L. and Van Griensven, A.: Can we trust remote sensing evapotranspiration products over Africa? Hydrology and Earth System Sciences, 24(3), pp.1565-1586, 2020.

Xue, J., Anderson, M. C., Gao, F., Hain, C., Yang, Y., Knipper, K. R., Kustas, W. P. and Yang, Y.: Mapping daily evapotranspiration at field scale using the harmonized landsat and sentinel-2 dataset, with sharpened VIIRS as a sentinel-2 thermal proxy. Remote Sensing, 13(17), p.3420, 2021.

860   Xue, J., Anderson, M. C., Gao, F., Hain, C., Knipper, K. R., Yang, Y., Kustas, W. P., Yang, Y., Bambach, N., McElrone, A. J. and Castro, S. J.: Improving the spatiotemporal resolution of remotely sensed ET information for water management through Landsat, Sentinel-2, ECOSTRESS and VIIRS data fusion. Irrigation Science, 40(4-5), pp.609-634, 2022.

Zhang, K., Kimball, J. S. and Running, S. W.: A review of remote sensing based actual evapotranspiration estimation. Wiley Interdisciplinary Reviews: Water, 3(6), pp.834-853, 2016.